The Motion of Mesoscale Snowbands in Northeast U.S. Winter Storms

JAYMES S. KENYON,[a] DANIEL KEYSER, AND LANCE F. BOSART

Department of Atmospheric and Environmental Sciences, University at Albany, State University of New York, Albany, New York

MICHAEL S. EVANS

NOAA/National Weather Service, Albany, New York

(Manuscript received 26 February 2019, in final form 6 November 2019)

ABSTRACT

The spatial distribution of snowfall accumulation accompanying winter storms is a product of both snowfall rate and duration. Winter storms are commonly associated with mesoscale snowbands that can strongly modulate snowfall accumulation. Although the development of mesoscale snowbands can usually be anticipated, snowband residence time at a fixed location is often a forecasting challenge. However, given that snowband residence time is related to characteristics of band motion, an improved understanding of band motion presents an opportunity to improve snowfall-accumulation forecasts. This study investigates environmental features associated with specific snowband motion characteristics. Using radar reflectivity data, snowband events in the northeast United States spanning a 6-yr period are categorized according to a band-motion classification scheme, with this scheme consisting of *laterally translating*, *hybrid*, *laterally quasi-stationary*, and *pivoting* snowbands. On the basis of this classification, composite analysis is performed to identify common environmental features associated with particular band-motion categories. Results indicate that snowband motion is related to cyclone-relative band position, the confluence/diffluence and curvature of midlevel streamlines, and the distribution of horizontal temperature advection. Snowband motion is also related to hodograph shape, as well as to the across- and along-isotherm components of the **Q** vector. Composite results are supplemented with case studies, which suggest that laterally quasi-stationary and pivoting snowbands can favor distinct gradients in snowfall accumulation. The present study proposes that snowband motion warrants consideration during the forecasting process and, to that end, conceptual models are presented to synthesize key findings for operational application.

1. Introduction

In the most rudimentary sense, forecasts of precipitation accumulation require the consideration of both precipitation rate and duration (e.g., Doswell et al. 1996; Evans and Jurewicz 2009). Mesoscale precipitation bands, hereafter called mesoscale bands, are frequently observed in conjunction with extratropical cyclones, and enhanced precipitation rates within mesoscale bands can have an appreciable impact on precipitation accumulation. Moreover, because mesoscale bands have inherently high aspect (length-to-width) ratios, precipitation duration at a fixed location may be strongly modulated by the component of band motion relative to the band axis,[1] and this motion can influence whether pronounced precipitation accumulation gradients are likely. Despite the potential importance of band motion on precipitation accumulation, forecasting approaches typically do not consider band motion and focus on assessing band position and precipitation rate.

Supplemental information related to this paper is available at the Journals Online website: https://doi.org/10.1175/WAF-D-19-0038.s1.

[a] Current affiliation: University of Colorado Boulder, Cooperative Institute for Research in Environmental Sciences, and NOAA/OAR/ESRL/Global Systems Division, Boulder, Colorado.

Corresponding author: Jaymes S. Kenyon, jaymes.kenyon@noaa.gov

[1] The term "axis," when used to describe the axis of a mesoscale band, is hereafter understood to refer to the major axis of the band.

Publisher's Note: This article was revised on 20 February 2020 to correct a typographical error that caused a misspelling in the Introduction.

DOI: 10.1175/WAF-D-19-0038.1

Previous literature on mesoscale bands is extensive, but contains comparatively limited information on band motion. Using radar observations, Harper and Beimers (1958) found that the movement of frontal precipitation "belts" was well described by the across-band component of the 700-hPa flow. Drawing from linear perturbation theory of symmetric instability, Seltzer et al. (1985) hypothesized that mesoscale bands will tend to move with the mean across-band component of the flow, and confirmed this movement in a sample of observed bands. Banacos (2003) postulated that regions of frontogenesis within nontranslating deformation zones would favor mesoscale bands that yield distinct precipitation accumulation gradients, while regions of frontogenesis within deformation zones that translate in a direction across their axes of dilatation would favor relatively brief banded precipitation at a fixed location. In their study of mesoscale bands in northeast U.S. winter storms, Novak et al. (2004) noted that a majority of bands in the northwest quadrants of cyclones exhibited a distinct "pivot point," with the bands pivoting as they translated with the parent system, and this pivot point was found to be a favored region for heavy precipitation accumulation. Furthermore, bands in other quadrants tended to move with the mean low- to midlevel flow in the vicinity of the band. In a recent study of northeast U.S. winter storms, Ganetis et al. (2018) found that mesoscale snowbands exhibiting along-axis motion are commonly observed in the northeast quadrant of developing surface cyclones, whereas snowbands exhibiting across-axis motion are commonly observed in the northwest quadrant of mature surface cyclones.

Given the potential importance of band motion on precipitation accumulation and the limited treatment of band motion in previous literature on mesoscale bands, this research investigates synoptic and mesoscale features associated with band motion characteristics observed in northeast U.S. winter storms. Mesoscale snowbands, as a subset of mesoscale bands, are the focus of this study, since snowfall is often associated with more extensive societal impacts than a mass-equivalent accumulation of rainfall. A snowband motion classification scheme, consisting of *laterally translating, hybrid, laterally quasi-stationary,* and *pivoting* snowband categories, is used to classify a sample of snowbands from a 6-yr period. From this classification, composite analyses and case studies are performed to examine environmental features commonly observed with particular categories of snowband motion, with emphasis on diagnostic fields that are routinely available to forecasters. Results are synthesized into conceptual models to facilitate the forecasting process when snowband development is expected.

2. Data and methods

a. Data sources

To begin a systematic identification of mesoscale snowbands for this study, the daily climatological records of all 39 Primary Local Climatological Data (PLCD; NWS 2018) sites throughout the northeast United States—encompassing a region from Maine to Virginia—were searched for occurrences of heavy snow accumulation during the 6-yr period spanning 2005–10. In consultation with NWS forecasters, heavy snow accumulation was defined as any amount $\geq$ 6 in. (15.2 cm) during a local calendar day (utilizing eastern standard time). Using this criterion, 136 dates were identified on which heavy snow accumulation occurred at one or more sites, and these dates were deemed heavy snow dates. The PLCD sites utilized in this study are listed in Table 1.

For each heavy snow date, radar reflectivity mosaics were constructed using the 0.5° elevation scan from 20 WSR-88D sites (Table 1) at 15-min intervals. These mosaics were rendered from NCEI Level III data using the GEMPAK (desJardins et al. 1991) "GDRADR" application with 1-km horizontal grid spacing. No objective quality control was applied. To infer precipitation type, mosaics were overlaid with present-weather symbols from hourly METAR reports (courtesy of Iowa State University, http://mesonet.agron.iastate.edu/archive/). From the mosaics, 40 heavy snow dates were subjectively identified as arising entirely from the occurrence of lake effect snowfall—either as "pure" lake-effect or as lake-effect-enhanced snowfall—at PLCD sites, and these dates were removed from further consideration. Allowing for multiday continuity of synoptic weather systems, the remaining 96 heavy snow dates were grouped into 71 heavy snow events (Table 2). Thus, each heavy snow event may be regarded as corresponding to a progressive synoptic-scale weather system that produced heavy snow within the northeast United States during the study period.

Gridded data from the CFSR (Saha et al. 2010) were obtained from NCEI for each of the 71 heavy snow events. The CFSR is a global dataset with 0.5° latitude–longitude horizontal grid spacing and is available at 6-hourly intervals (i.e., 0000, 0600, 1200, and 1800 UTC, hereafter called analysis times). All diagnostic fields in this study have been calculated and plotted from the CFSR dataset using GEMPAK applications.

b. Methods

1) Snowband identification and classification

For each heavy snow event, animated reflectivity mosaics and hourly METAR reports were used to

TABLE 1. Listing of the 39 PLCD sites and 20 WSR-88D radars utilized in this study, grouped by state/district.

State/district	PLCD sites (identifier in parentheses)	WSR-88D radars (identifier in parentheses)
Connecticut	Bridgeport (KBDR)	
	Hartford (KHFD)	
Delaware	Wilmington (KILG)	Dover Air Force Base (KDOX)
District of Columbia	Washington (KDCA)	
Maine	Caribou (KCAR)	Caribou (KCBW)
	Portland (KPWM)	Portland (KGYX)
Maryland	Baltimore (KBWI)	
Massachusetts	Boston (KBOS)	Boston (KBOX)
	Worcester (KORH)	
New Hampshire	Concord (KCON)	
New Jersey	Atlantic City (KACY)	Fort Dix (KDIX)
	Newark (KEWR)	
New York	Albany (KALB)	Albany (KENX)
	Binghamton (KBGM)	Binghamton (KBMX)
	Buffalo (KBUF)	Buffalo (KBUF)
	Islip (KISP)	Fort Drum (KTYX)
	Ithaca (KITH)	Upton (KOKX)
	New York/Central Park (KNYC)	
	New York/JFK (KJFK)	
	New York/LaGuardia (KLGA)	
	Rochester (KROC)	
North Carolina	None included; radar sites only	Morehead City (KMHX)
		Raleigh (KRAX)
		Wilmington (KLTX)
Pennsylvania	Allentown (KABE)	Pittsburgh (KPBZ)
	Erie (KERI)	State College (KCCX)
	Harrisburg (KCXY)	
	Philadelphia (KPHL)	
	Pittsburgh (KPIT)	
	Scranton (KAVP)	
	Williamsport (KIPT)	
Rhode Island	Providence (KPVD)	
Vermont	Burlington (KBTV)	Burlington (KCXX)
Virginia	Washington/Dulles (KIAD)	Norfolk (KAKQ)
	Lynchburg (KLYH)	Roanoke (KFCX)
	Norfolk (KORF)	Sterling (KLWX)
	Richmond (KRIC)	
	Roanoke (KROA)	
West Virginia	Beckley (KBKW)	Charleston (KRLX)
	Charleston (KCRW)	
	Elkins (KEKN)	
	Huntington (KHTS)	

subjectively identify mesoscale snowbands within the mosaic domain that coincided with analysis times. Mesoscale snowbands were identified when the following criteria were satisfied:

1) A single-banded feature in reflectivity, characterized by an aspect ratio of $\geq$ 4:1 at the 20-dBZ threshold.
2) Within the banded feature, an embedded region of reflectivity $\geq$ 25 dBZ along at least half of the axis and $\geq$10 dBZ over the background reflectivity, without the requirement that this region be continuous.
3) Persistence of criteria 1 and 2 for $\geq$3 h. This persistence period may begin at, be inclusive of, or end at the analysis time.
4) Observed snow at the surface (per METAR reports) at any time during the period satisfying criterion 3 and along any segment of the banded feature.

The presence of a snowband within the reflectivity mosaic domain at an analysis time constituted a snowband event, uniquely identified by time and location. Note that a heavy snow event may be associated with one or several snowband events, or merely exhibit nonbanded or weakly banded precipitation. Similar criteria for aspect ratio, reflectivity, and persistence have been used by Novak et al. (2004, 2006) and Baxter and Schumacher (2017) for subjective identification of single mesoscale bands.

TABLE 2. Listing of 71 heavy snow events and their 96 associated heavy snow dates.

Heavy snow event No.	Heavy snow date(s)	Heavy snow event No.	Heavy snow date(s)
1	5 Jan 2005	41	13 Feb 2008
	6 Jan 2005	42	22 Feb 2008
2	19 Jan 2005	43	26 Feb 2008
	20 Jan 2005		27 Feb 2008
3	22 Jan 2005	44	1 Mar 2008
	23 Jan 2005	45	7 Mar 2008
4	26 Jan 2005		8 Mar 2008
5	10 Feb 2005	46	20 Mar 2008
	11 Feb 2005	47	25 Nov 2008
6	21 Feb 2005	48	12 Dec 2008
7	24 Feb 2005	49	19 Dec 2008
8	28 Feb 2005	50	21 Dec 2008
	1 Mar 2005		22 Dec 2008
9	8 Mar 2005	51	10 Jan 2009
10	11 Mar 2005		11 Jan 2009
	12 Mar 2005	52	18 Jan 2009
11	23 Mar 2005	53	28 Jan 2009
12	3 Apr 2005	54	3 Feb 2009
13	9 Dec 2005	55	22 Feb 2009
14	16 Dec 2005		23 Feb 2009
15	25 Dec 2005	56	2 Mar 2009
	26 Dec 2005	57	22 Oct 2009
16	3 Jan 2006	58	9 Dec 2009
17	23 Jan 2006	59	18 Dec 2009
18	11 Feb 2006		19 Dec 2009
	12 Feb 2006		20 Dec 2009
19	25 Feb 2006	60	23 Dec 2009
20	2 Mar 2006	61	2 Jan 2010
21	4 Mar 2006		3 Jan 2010
22	6 Feb 2007	62	9 Jan 2010
23	14 Feb 2007	63	18 Jan 2010
24	2 Mar 2007	64	30 Jan 2010
25	16 Mar 2007	65	5 Feb 2010
	17 Mar 2007		6 Feb 2010
26	4 Apr 2007	66	9 Feb 2010
	5 Apr 2007		10 Feb 2010
27	13 Apr 2007	67	16 Feb 2010
28	16 Apr 2007	68	23 Feb 2010
	17 Apr 2007		24 Feb 2010
29	3 Dec 2007	69	25 Feb 2010
30	5 Dec 2007		26 Feb 2010
31	13 Dec 2007	70	16 Dec 2010
32	16 Dec 2007	71	26 Dec 2010
	17 Dec 2007		27 Dec 2010
33	20 Dec 2007		
34	31 Dec 2007		
35	1 Jan 2008		
36	14 Jan 2008		
37	18 Jan 2008		
38	1 Feb 2008		
39	5 Feb 2008		
40	6 Feb 2008		

To proceed with an investigation of snowband motion, the subjective snowband motion classification scheme proposed by Kenyon (2013, section 2.2.1) was utilized. This scheme permits the classification of a large population of snowband events into relatively few categories while making operationally meaningful distinctions concerning snowband motion. The classification scheme consists of four categories of snowband motion: laterally translating, hybrid, laterally quasi-stationary, and pivoting. These snowband motion categories within the hierarchy of heavy snow events and snowband events are shown in Fig. 1a. Laterally translating snowbands exhibit predominantly across-axis motion, thereby favoring uniform snowfall accumulation within the regions they traverse. In contrast to laterally translating snowbands, laterally quasi-stationary snowbands exhibit near-zero across-axis motion, regardless of the magnitude of along-axis motion. Hybrid snowbands combine the motion attributes of laterally quasi-stationary and laterally translating snowbands, exhibiting across- and along-axis components of motion concurrently. Finally, pivoting snowbands exhibit pronounced rotation, such that a segment of the band near the center of rotation, to be referred to as the pivot zone (PZ), exhibits near-zero across-axis motion. The criteria used to define these band motion categories are illustrated in Fig. 1b.

The snowband motion classification scheme was subjectively applied to each snowband event using the following procedure:

1) A 1-h period was chosen during which band motion could be observed in reflectivity mosaics. Preferentially, this period was centered on the analysis time associated with the snowband event. However, if during this period band reflectivity changes were rapid or the band was near the edge of the mosaic domain, the 1-h period was recentered either forward or backward, but with the requirement that this period begin with, end at, or be inclusive of the analysis time. If significant radar coverage gaps precluded satisfactory tracking of the candidate snowband, the snowband event was deemed unclassifiable.
2) A reflectivity value ($\geq$20 dBZ) representative of the band outline during the 1-h period was identified to the nearest 5 dBZ. Typically, the 20-dBZ value provided a representative band outline.
3) If a PZ was observed during the 1-h period, the snowband event was assigned to the pivoting category. The location of the PZ was recorded to the nearest 0.2° of latitude and longitude, along with the azimuthal orientation of the band at the PZ to the nearest 5°.
4) If no PZ was observed during the 1-h period, band centroid locations were determined by identifying the approximate midpoint of the band axis at both

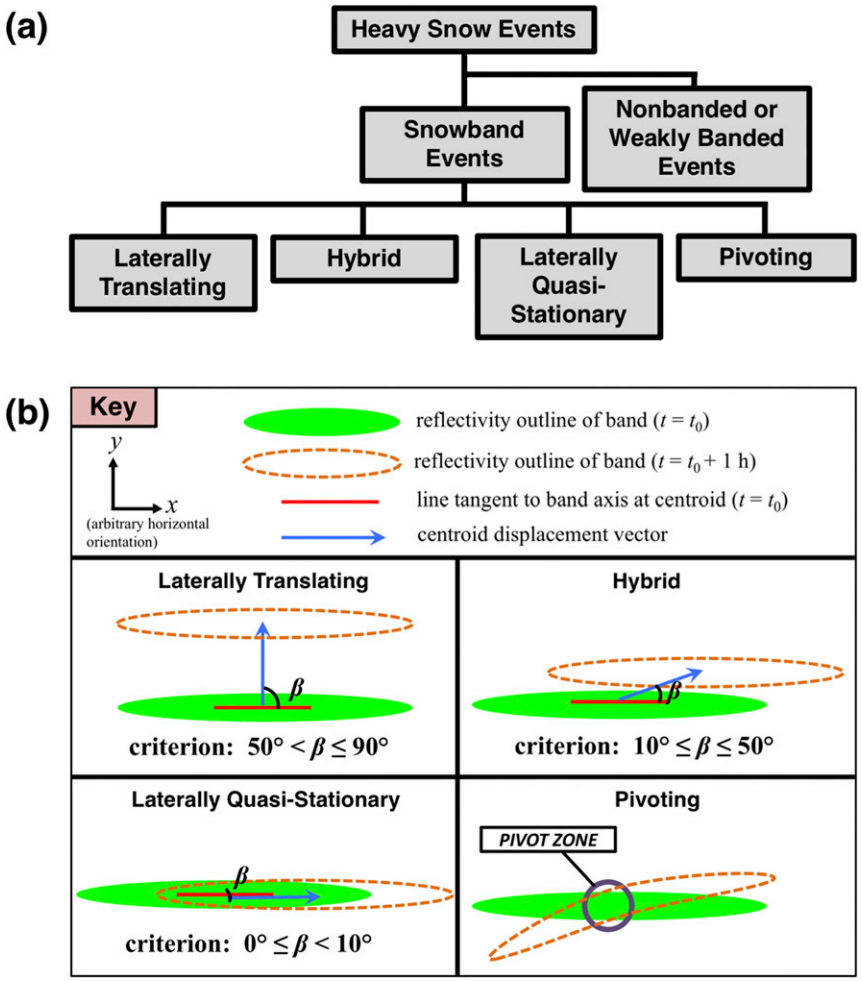

FIG. 1. (a) Flowchart of the snowband motion classification scheme used in this study. (b) Schematic representations of the four snowband motion categories and their defining criteria. The start of the 1-h period during which band motion is evaluated is denoted by t_0. Angle β is a measure of the across-axis component of band motion.

the starting and ending times. From these two locations, a 1-h centroid displacement vector was constructed. Next, the angle (denoted as β) between this vector and the line tangent to the band axis at the initial location of the centroid was measured to the nearest 10°, such that β provided a metric of relative across-axis, or lateral, motion. The band was then classified according to the criteria in Fig. 1b. The location of the centroid at the analysis time and the azimuthal orientation of the band at the centroid were also recorded.

Pivoting snowbands, although exhibiting a PZ during a 1-h observing period, would often undergo translation. Thus, the PZ was often found to be a nonstationary feature when pivoting snowbands were observed over several hours. For simplicity, the PZ is regarded as analogous to a band centroid—namely, as a feature along a snowband that is identifiable at a given time.

2) DIAGNOSTIC METHODS

Mesoscale bands that are forced by frontogenesis are a manifestation of vertical circulations transverse to frontal zones, hereafter referred to as frontal circulations. Such bands are commonly observed to be oriented approximately parallel to frontal zones, as predicted by theoretical studies of frontogenetically forced vertical circulations (e.g., Sawyer 1956; Eliassen 1962). The **Q** vector (Hoskins et al. 1978; Hoskins and Pedder 1980) is pertinent to the relationship between band orientation and frontal-zone orientation, as the **Q** vector is related to the quasi-geostrophic (QG) forcing of vertical motion in general, including the QG forcing of frontal circulations, without

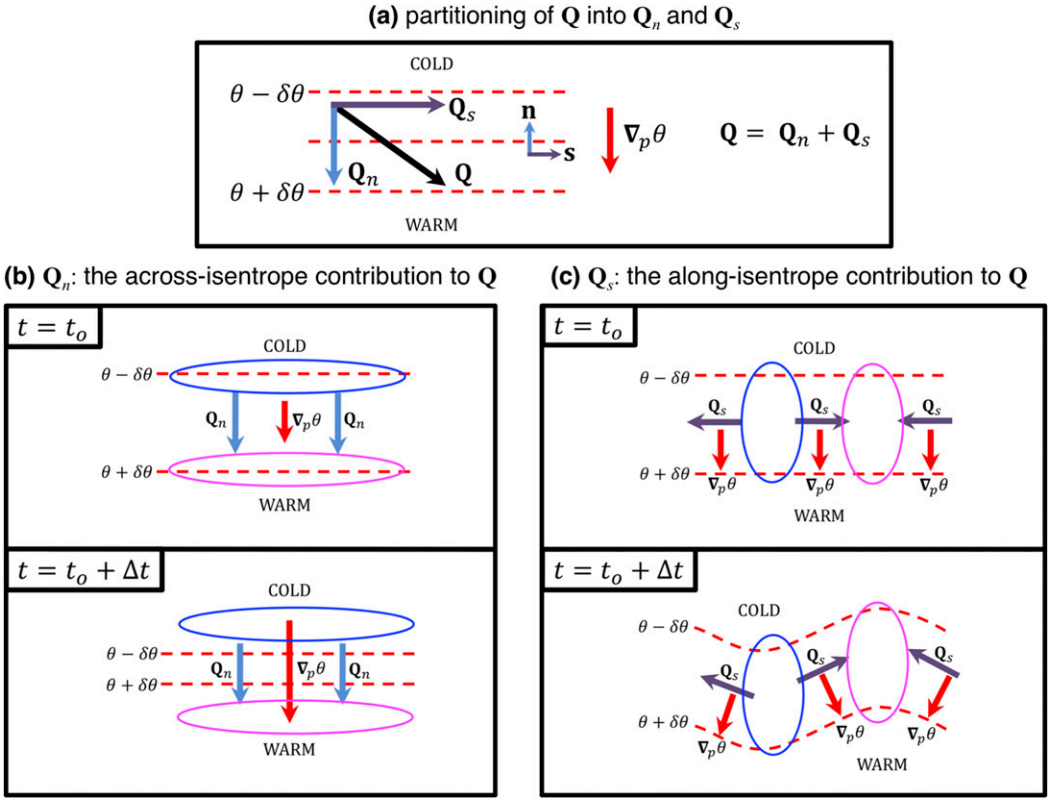

FIG. 2. (a) Schematic illustration of a natural-coordinate partitioning of **Q** into across- and along-isentrope contributions, $\mathbf{Q}_n$ and $\mathbf{Q}_s$, respectively [adapted from Fig. 12 in Martin (1999)]. (b) Schematic illustration of the effect of $\mathbf{Q}_n$ on $\nabla_p\theta$ during an interval of time. An increase in $|\nabla_p\theta|$ by the geostrophic wind occurs where $\mathbf{Q}_n$ is directed toward warmer air. Regions of $\mathbf{Q}_n$ convergence (divergence) are shown in magenta (blue). (c) Schematic illustration of the effect of $\mathbf{Q}_s$ on $\nabla_p\theta$ during an interval of time. A counterclockwise (clockwise) rotation of $\nabla_p\theta$ by the geostrophic wind occurs where $\mathbf{Q}_s$ is directed downshear (upshear). Regions of $\mathbf{Q}_s$ convergence (divergence) are shown in magenta (blue).

restriction to the canonical configurations of frontogenesis considered by Sawyer (1956) and Eliassen (1962).

The **Q** vector (**Q**) is defined as the temporal rate of change of $\nabla_p\theta$ following a trajectory defined by the geostrophic wind [e.g., Eq. (1.5) in Keyser et al. (1988)]. To separately diagnose the temporal rates of change of the magnitude and direction of $\nabla_p\theta$ that are encapsulated in **Q**, a natural-coordinate partitioning of **Q** is employed following Keyser et al. (1988). In this partitioning, $\nabla_p\theta$ is used to define a unit vector $\mathbf{n} = -|\nabla_p\theta|^{-1}\nabla_p\theta$, which is directed normal to the local isentrope toward colder air. A second unit vector, $\mathbf{s} = \mathbf{n} \times \mathbf{k}$, is directed tangent to the local isentrope in the downshear direction, where shear is hereafter understood to be the vertical shear ascribed to the thermal wind.[2] The unit vectors **n** and **s** are then used to define a natural-coordinate system (n, s) in which **Q** is partitioned:

$$\mathbf{Q} = Q_n\mathbf{n} + Q_s\mathbf{s}, \tag{1a}$$

or alternatively,

$$\mathbf{Q} = \mathbf{Q}_n + \mathbf{Q}_s, \tag{1b}$$

where $\mathbf{Q}_n \equiv Q_n\mathbf{n}$ and $\mathbf{Q}_s \equiv Q_s\mathbf{s}$ are the across- and along-isentrope contributions to **Q**, respectively. This natural-coordinate partitioning, illustrated schematically in Fig. 2a, will be used to diagnose kinematic properties and patterns of vertical-motion forcing that distinguish laterally translating, laterally quasi-stationary, and pivoting snowbands. Because neither a composite nor a case study will be presented for the hybrid snowband category (the rationale for the exclusion of which will be explained in the next subsection), the partitioning of **Q** will not be considered for this band-motion category.

[2] The stated relationship between the **s** direction and the downshear direction is understood to apply to the Northern Hemisphere.

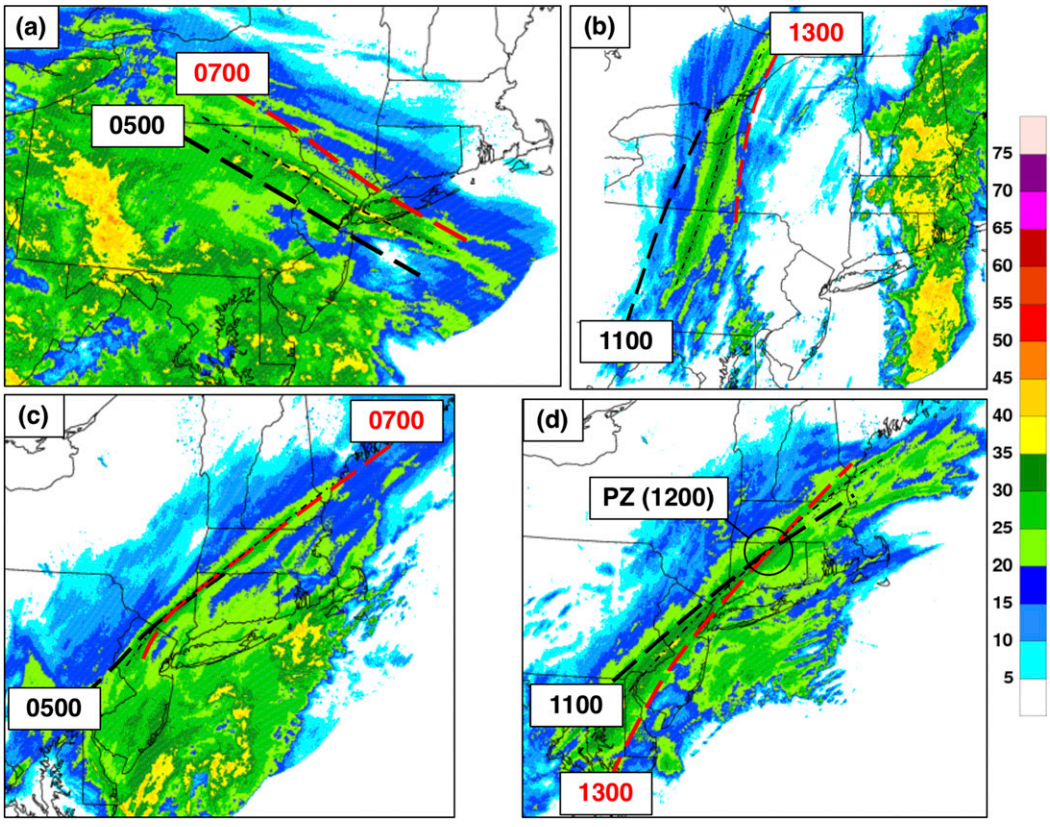

FIG. 3. Radar reflectivity (dBZ) mosaics from the 0.5° elevation scan for (a) a laterally translating snowband event at 0600 UTC 9 Dec 2009, (b) a hybrid snowband event at 1200 UTC 12 Dec 2008, (c) a laterally quasi-stationary snowband event at 0600 UTC 2 Mar 2009, and (d) a pivoting snowband event at 1200 UTC 12 Feb 2006. In each panel, the dash–dot pattern denotes the axis of the snowband at the mosaic time, and dashed black (dashed red) denotes the position of the band axis 1-h before (after) the mosaic time, as labeled. In (d), the encircled region marked ''PZ (1200)'' denotes the location of the PZ at the mosaic time. Animated reflectivity mosaics for each of these snowband events are provided in the online supplemental material.

The temporal rate of change of $|\nabla_p\theta|$ as effected by the geostrophic wind is quantified by Q_n. An increase (decrease) in $|\nabla_p\theta|$ by the geostrophic wind occurs where $\mathbf{Q}_n$, the across-isentrope contribution to $\mathbf{Q}$, is directed toward warmer (colder) air (Fig. 2b). The quantity $\nabla_p \cdot \mathbf{Q}_n$ represents the QG forcing of vertical motion associated with frontal circulations, and patterns of $\nabla_p \cdot \mathbf{Q}_n$ are typically manifested as elongated regions along frontal zones (Keyser et al. 1988, 1992), as shown schematically in Fig. 2b. The temporal rate of change of the direction of $\nabla_p\theta$ as effected by the geostrophic wind is quantified by Q_s. A counterclockwise (clockwise) rotation of $\nabla_p\theta$ by the geostrophic wind occurs where $\mathbf{Q}_s$, the along-isentrope contribution to $\mathbf{Q}$, is directed downshear (upshear) (Fig. 2c). The quantity $\nabla_p \cdot \mathbf{Q}_s$ represents the QG forcing of vertical motion associated with synoptic-scale disturbances, and patterns of $\nabla_p \cdot \mathbf{Q}_s$ are typically manifested as cellular regions (Keyser et al. 1988, 1992), as shown schematically in Fig. 2c.

QG diagnostic fields calculated from high-resolution gridded datasets (such as the CFSR) are prone to exhibiting substantial noise. To render coherent fields of $\mathbf{Q}$ vectors and their divergence, $\mathbf{Q}$ vectors are calculated by first applying a Gaussian smoothing operator to the horizontal potential temperature field, and then substituting the nondivergent wind in place of the geostrophic wind. Nielsen-Gammon and Gold (2008, section 2) demonstrate that this substitution in the calculation of QG diagnostics from high-resolution gridded datasets yields more coherent diagnostic fields, and they argue that this substitution ''is fully consistent with quasigeostrophic theory ... and allows more aspects of the balanced dynamics to be retained and diagnosed'' (p. 184). On the basis of these considerations, $\mathbf{Q}$ vectors are diagnosed using the nondivergent wind in place of the geostrophic

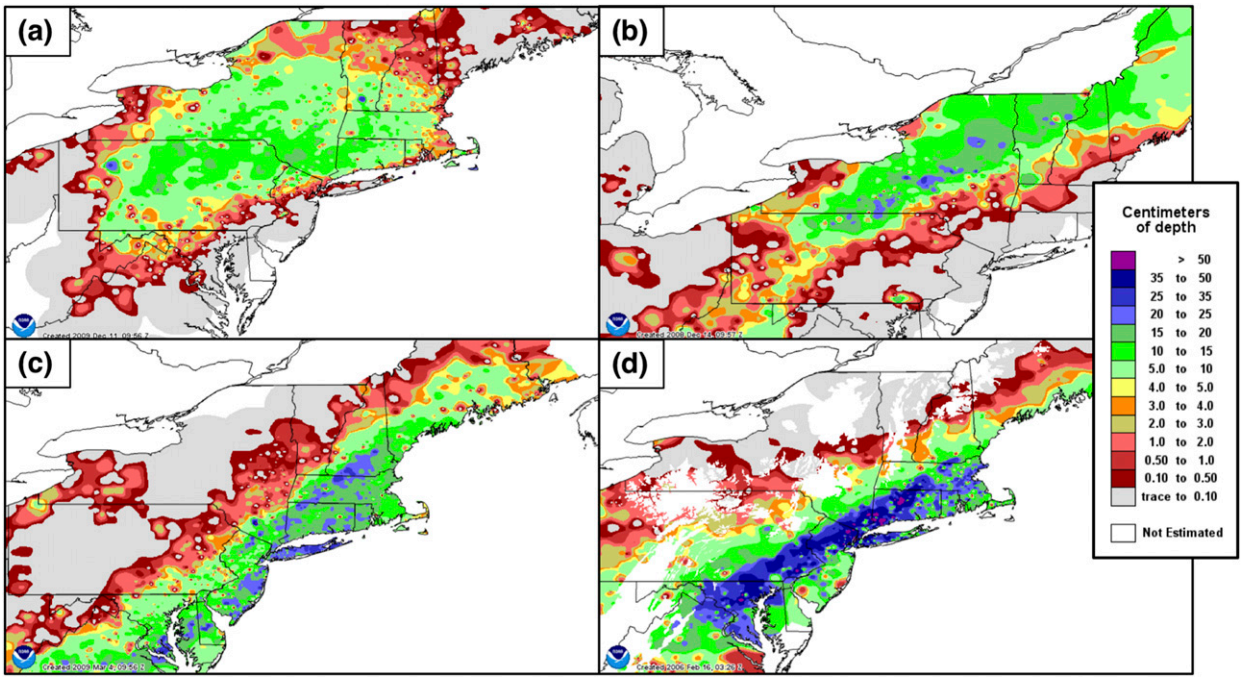

FIG. 4. The 24-h snowfall accumulation (cm) associated with the snowband events in Fig. 3. The 24-h ending times are (a) 1200 UTC 9 Dec 2009, (b) 1800 UTC 12 Dec 2008, (c) 1200 UTC 2 Mar 2009, and (d) 1800 UTC 12 Feb 2006.

wind and the associated **Q**-vector divergence serves as a surrogate for the QG forcing of vertical motion. To diagnose frontogenesis by the total horizontal wind, the 2D form of the Miller (1948) frontogenesis equation is utilized [e.g., Eq. (1) in Novak et al. (2004)], and in subsequent sections, the term *frontogenesis* will refer to Miller 2D frontogenesis. Note that the Miller 2D frontogenesis equation, when evaluated using the nondivergent wind, is equivalent to $-Q_n$.

3) COMPOSITE ANALYSIS AND CASE STUDIES

Composite averages of diagnostic fields were calculated for the laterally translating, laterally quasi-stationary, and pivoting band motion categories in order to ascertain common environmental features associated with these categories. Hybrid snowbands, characterized by intermediate values of β (refer to Fig. 1b), were found in various synoptic environments. For this reason, a hybrid category composite was not constructed.

Given that the snowband events belonging to a given category were observed in various locations, a band-centered compositing approach was utilized. In this approach, band centers were defined as the band centroid for laterally translating and laterally quasi-stationary bands, and the PZ for pivoting bands. Composite calculations then proceeded by recentering bands onto the location of Albany, New York (chosen arbitrarily), before averaging variables across member events. Composites of diagnostic fields were obtained by first calculating the field for each snowband event and then averaging the field across member events. For each composite category, only bands whose azimuthal orientations were within 20° of the category mean were retained for compositing. This requirement ensured that along- and across-band variations in the composited fields would not be excessively smoothed due to differences in member-band orientations. Supplemental composite fields, beyond those that will be presented in section 3, may be accessed in the online supplemental material and are available in Kenyon (2013, section 3.2).

Radar reflectivity mosaics depicting snowband events for each of the four motion categories are shown in Fig. 3 (animations of the reflectivity mosaics for the respective motion categories are provided in the online supplemental material). To convey a sense of band motion, each panel in Fig. 3 is annotated with band positions 1-h before and after the mosaic time. Figure 4 depicts the 24-h snowfall accumulation associated with the snowband events in Fig. 3, as obtained from the National Operational Hydrologic Remote Sensing Center (http://www.nohrsc.noaa.gov). For consistency, each of the 24-h accumulation periods in Fig. 4 ends 6 h after the respective mosaic time in Fig. 3.

The laterally translating, laterally quasi-stationary, and pivoting snowband events (Figs. 3a,c,d, respectively),

TABLE 3. Catalog of snowband events assigned to each category of snowband motion. Dates preceded by a double asterisk are recorded as being one day after the corresponding heavy snow date in Table 2, owing to the time difference between eastern standard time and UTC. Time entries in bold indicate snowband events that were excluded from their respective category composite. Time entries appended with a single asterisk denote snowband events presented as case studies.

Laterally translating (19 events overall, 17 events in composite)					Hybrid (7 events overall)				Laterally quasi-stationary (9 events overall, 8 events in composite)					Pivoting (26 events overall, 18 events in composite)			
Date	Time (UTC)	Band centroid location (lat, lon) (°N, °W)	Azimuthal orientation of band at centroid (° clockwise from local meridian)	Angle β (°)	Date	Time (UTC)	Azimuthal orientation of band at centroid (° clockwise from local meridian)	Angle β (°)	Date	Time (UTC)	Band centroid location (lat, lon) (°N, °W)	Azimuthal orientation of band at centroid (°clockwise from local meridian)	Angle β (°)	Date	Time (UTC)	Pivot zone location (lat, lon) (°N, °W)	Azimuthal orientation of band at pivot zone (° clockwise from local meridian)
28 Feb 2005	1800	39.6, 74.2	110	70	8 Mar 2005	1800	20	30	16 Mar 2007	1200	41.4, 73.2	50	<10	20 Jan 2005	**1200**	45.8, 68.2	10
1 Mar 2005	**0000**	41.4, 71.6	80	80	**6 Dec 2007	0000	60	50	13 Feb 2008	1200	41.0, 80.2	40	<10		1800	45.8, 67.0	50
	0600	43.2, 69.2	60	80	6 Feb 2008	0600	80	30		1200	42.8, 76.6	40	<10	22 Jan 2005	**1800**	43.4, 79.2	75
9 Dec 2005	0600	42.4, 75.8	115	70		1200	90	30	22 Feb 2008	**1800**	40.8, 80.4	70	<10	23 Jan 2005	1200	43.6, 69.2	60
2 Mar 2007	1200	44.8, 70.0	120	80	12 Dec 2008	1200	10	40	**23 Feb 2008	0000	42.0, 73.8	65	<10	1 Mar 2005	1200	43.8, 71.0	40
16 Dec 2007	1800	45.2, 68.2	110	70	28 Jan 2009	0600	120	40	8 Mar 2008	1200	43.8, 78.2	40	<10	9 Dec 2005	1800	43.8, 69.8	55
**2 Feb 2008	0000	46.4, 66.8	120	90	2 Mar 2009	1800	10	20	12 Dec 2008	0600	44.4, 75.2	45	<10	12 Feb 2006	0600	39.0, 77.4	40
13 Feb 2008	0600	44.4, 70.8	120	90					3 Feb 2009	1200	41.6, 70.4	35	<10		1200*	41.8, 72.8	50
	1200	46.2, 67.0	110	70					2 Mar 2009	0600*	42.0, 73.0	50	<10		1800	43.0, 70.8	50
27 Feb 2008	0000	43.6, 70.2	115	90										2 Mar 2006	**1800**	42.6, 74.8	100
	0600	44.8, 67.2	90	90					Category mean (all bands):			48		14 Feb 2007	1800	42.0, 75.2	35
**2 Mar 2008	0000	46.6, 66.8	100	90					Category mean (composited bands):			46		17 Mar 2007	0600	43.4, 75.8	40
21 Dec 2008	1200	43.6, 75.2	120	80										16 Apr 2007	**0600**	41.0, 76.2	0
9 Dec 2009	0600*	41.0, 74.4	120	80										14 Jan 2008	1800	44.4, 69.8	40
	1800	45.4, 69.2	120	80										27 Feb 2008	1200	46.2, 67.2	45
5 Feb 2010	1800	39.8, 80.4	105	80										22 Dec 2008	0000	44.6, 71.0	45
	1800	38.2, 79.4	120	80										23 Feb 2009	0600	45.2, 69.6	50
6 Feb 2010	0000	39.6, 75.4	120	80										19 Dec 2009	1200	38.6, 80.2	55
	0000	38.0, 75.4	125	80										20 Dec 2009	0600	41.4, 72.4	40
															1200	42.8, 71.2	25
Category mean (all bands):			109											6 Feb 2010	**0600**	41.0, 80.4	105
Category mean (composited bands):			114												**1800**	40.4, 73.4	75
														26 Dec 2010	1800	37.8, 75.6	30
														27 Dec 2010	**0000**	39.6, 74.4	0
															0600	41.2, 74.2	20
															1200	45.0, 70.4	40
														Category mean (all bands):			45
														Category mean (composited bands):			44

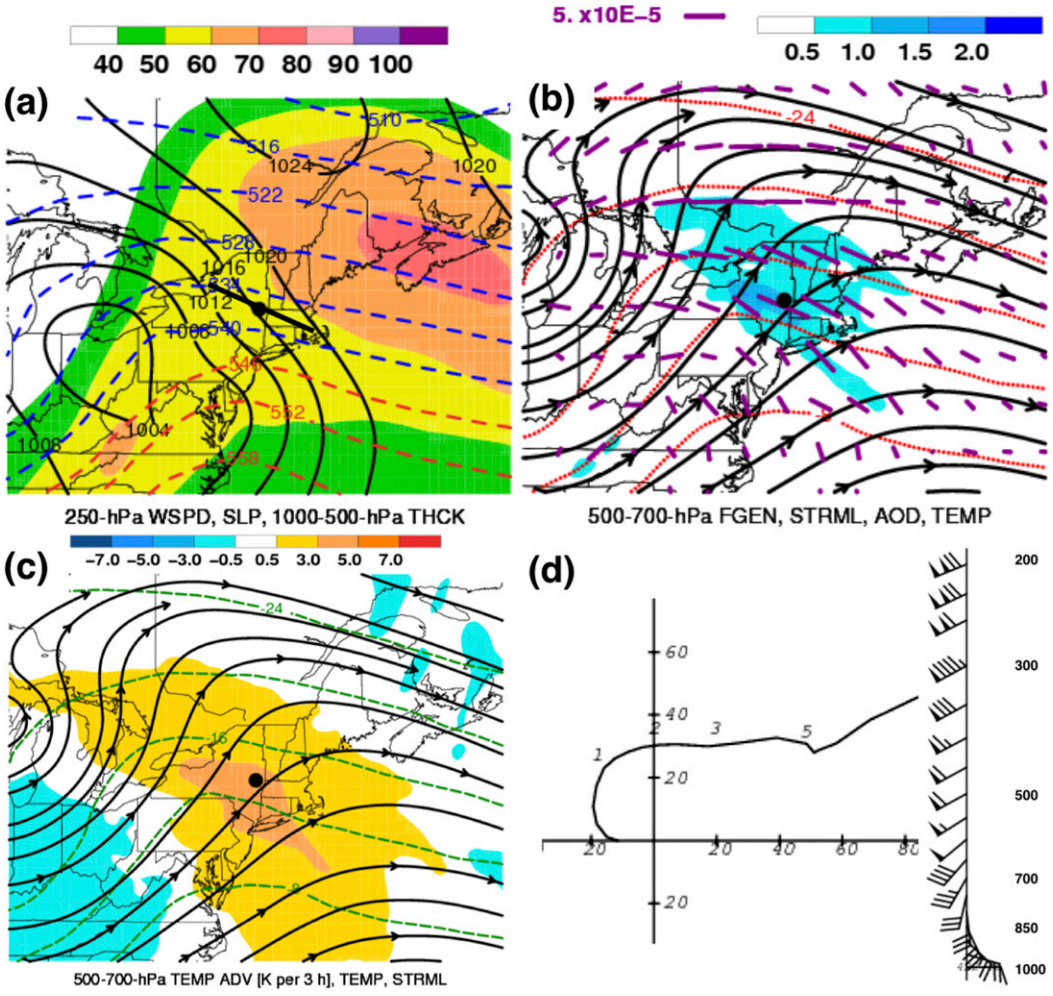

FIG. 5. Laterally translating category composite ($N = 17$) (a) MSLP (black solid, every 4 hPa), 1000–500-hPa thickness (blue dashed for ≤540 dam, red dashed otherwise, every 6 dam), and 250-hPa wind speed (shaded according to scale; m s^{-1}); (b) 700–500-hPa layer-mean streamlines (black solid with arrows), temperature (red dotted, every 4°C), axes of dilatation [purple tick marks, length scaled by resultant deformation, reference axis (5×10^{-5} s^{-1}) at top left], and Miller 2D frontogenesis [shaded according to scale; K (100 km)$^{-1}$ (3 h)$^{-1}$]; (c) 700–500-hPa layer-mean streamlines (black solid with arrows), temperature (green dashed, every 4°C), and horizontal temperature advection [shaded according to scale; K (3 h)$^{-1}$]; (d) hodograph at the band centroid location [heights labeled in km AGL, axes labeled in kt (1 kt ≈ 0.51 m s^{-1})], with the corresponding wind profile (wind barbs in kt using standard convention; axis in hPa) at right. In (a)–(c), the heavy black dot marks the band centroid location. In (a), the black line segment intersecting the band centroid location is of arbitrary length and the azimuthal orientation of the segment corresponds to that of the composite-mean band at the centroid.

along with important aspects of the snowfall accumulation attending these snowband events (Figs. 4a,c,d, respectively), will be discussed as case studies. Each of these snowband events has been subjectively selected for case study based upon the requirement that its diagnostic fields strongly resemble those of its respective category composite. Because a hybrid category composite was not constructed, a case study for the hybrid snowband event depicted in Fig. 3b will not be presented here, but is documented in Kenyon (2013, section 3.3.4). Note that the hybrid snowband event depicted in Fig. 3b is characterized by band motion that exhibits significant along- and across-axis components. Accordingly, gradients of snowfall accumulation shown in Fig. 4b (i.e., associated with the hybrid snowband) are generally sharper than those in Fig. 4a (i.e., associated with a laterally translating snowband), but are generally not as sharp as those in Figs. 4c and 4d (i.e., associated with laterally quasi-stationary and pivoting snowbands, respectively).

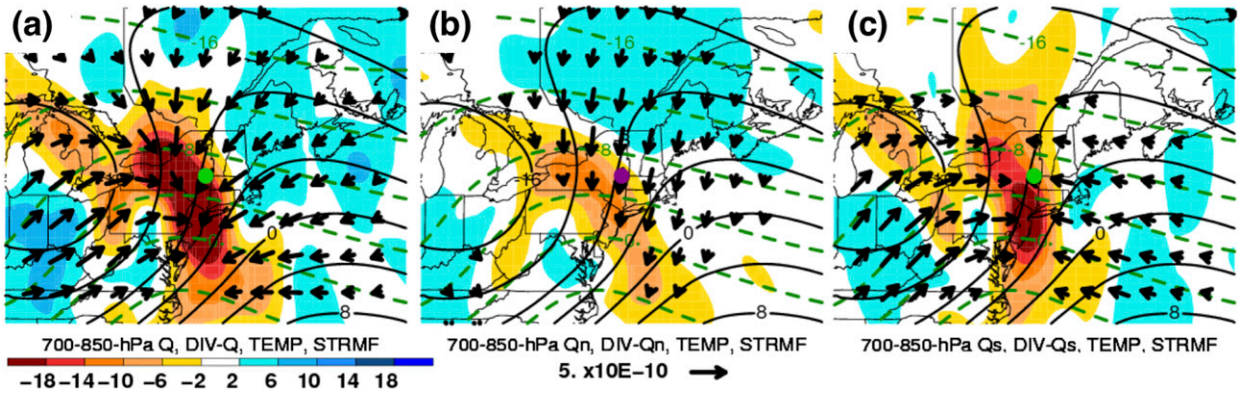

FIG. 6. Laterally translating category composite ($N = 17$) 850–700-hPa layer-mean (a) $\mathbf{Q}$ [black arrows, magnitudes $\geq 1 \times 10^{-10}$ K m^{-1} s^{-1}; reference vector (5×10^{-10} K m^{-1} s^{-1}) beneath (b)], $\mathbf{Q}$ divergence (shaded according to scale; 10^{-16} K m^{-2} s^{-1}), streamfunction (black solid, every 4×10^{6} m^{2} s^{-1}), and temperature (green dashed, every 4°C); (b) as in (a) except for $\mathbf{Q}_n$; (c) as in (a), except for $\mathbf{Q}_s$. In all panels, the heavy dot (green or purple) marks the band centroid location.

From the 71 heavy snow events, 66 snowband events were identified. Five of the 66 snowband events were deemed unclassifiable, with the remaining 61 snowband events cataloged in Table 3. Pivoting snowbands (26 events) were the most predominant type of snowband, followed by laterally translating (19 events), laterally quasi-stationary (nine events), and hybrid snowbands (seven events). The azimuthal-orientation requirement for compositing eliminated selected snowband events from each of the composited categories (i.e., the bolded time entries in Table 3), and resulted in a retention rate of 89% for the laterally translating and laterally quasi-stationary category composites, and 69% for the pivoting category composite.

3. Results

a. Composite analysis

1) LATERALLY TRANSLATING CATEGORY COMPOSITE

The centroid of the composite laterally translating snowband is located ~800 km east-northeast of the center of a surface cyclone and within the equatorward entrance region of a west-northwest–east-southeast-oriented 250-hPa jet streak (Fig. 5a). The configuration of 1000–500-hPa thickness contours at the centroid implies an approximately west-northwest–east-southeast band orientation (Fig. 5a), which closely aligns with the composite-mean band orientation (i.e., 114° clockwise from the local meridian; Table 3). Frontogenesis in the 700–500-hPa layer near the centroid is associated with deformation in diffluent southwesterly flow (Fig. 5b). All bands in the composite are observed to move in a poleward direction (i.e., toward colder air), and this motion is associated with the large across-band component of the 700–500-hPa flow that may be inferred from Fig. 5b. The centroid is located within a region of 700–500-hPa warm advection and immediately poleward of a warm-advection maximum (Fig. 5c). As implied by the thermal wind, the vertical wind profile at the centroid exhibits veering with height (Fig. 5d).

In the vicinity of the centroid of the composite laterally translating snowband, 850–700-hPa $\mathbf{Q}$ exhibits both across- and along-isotherm contributions, and $\nabla_p \cdot \mathbf{Q}$ attains large magnitudes relative to background values (Fig. 6a). The orientation of $\mathbf{Q}_n$ toward warmer air in the vicinity of the centroid indicates that the nondivergent wind contributes to an increase of $|\nabla_p \theta|$, and the elongated region of $\mathbf{Q}_n$ convergence provides QG forcing of ascent associated with a frontal circulation (Fig. 6b; compare the distribution of $\mathbf{Q}_n$ convergence with its counterpart in Fig. 2b, lower panel). The orientation of $\mathbf{Q}_s$ in the region upshear (downshear) of the centroid indicates a counterclockwise (clockwise) rotation of $\nabla_p \theta$ by the nondivergent wind, yielding a region of $\mathbf{Q}_s$ convergence that encompasses the centroid (Fig. 6c; compare the distribution of $\mathbf{Q}_s$ convergence with its counterpart in Fig. 2c, lower panel). Within this region of $\mathbf{Q}_s$ convergence and near the centroid, the magnitude of $\mathbf{Q}_s$ is small relative to where $\mathbf{Q}_s$ is oriented downshear and upshear surrounding the centroid (Fig. 6c), indicative of a relatively weak rotation of $\nabla_p \theta$ by the nondivergent wind.

2) LATERALLY QUASI-STATIONARY CATEGORY COMPOSITE

The centroid of the composite laterally quasi-stationary snowband is located ~700 km north-northeast of the center of a surface cyclone and within the equatorward

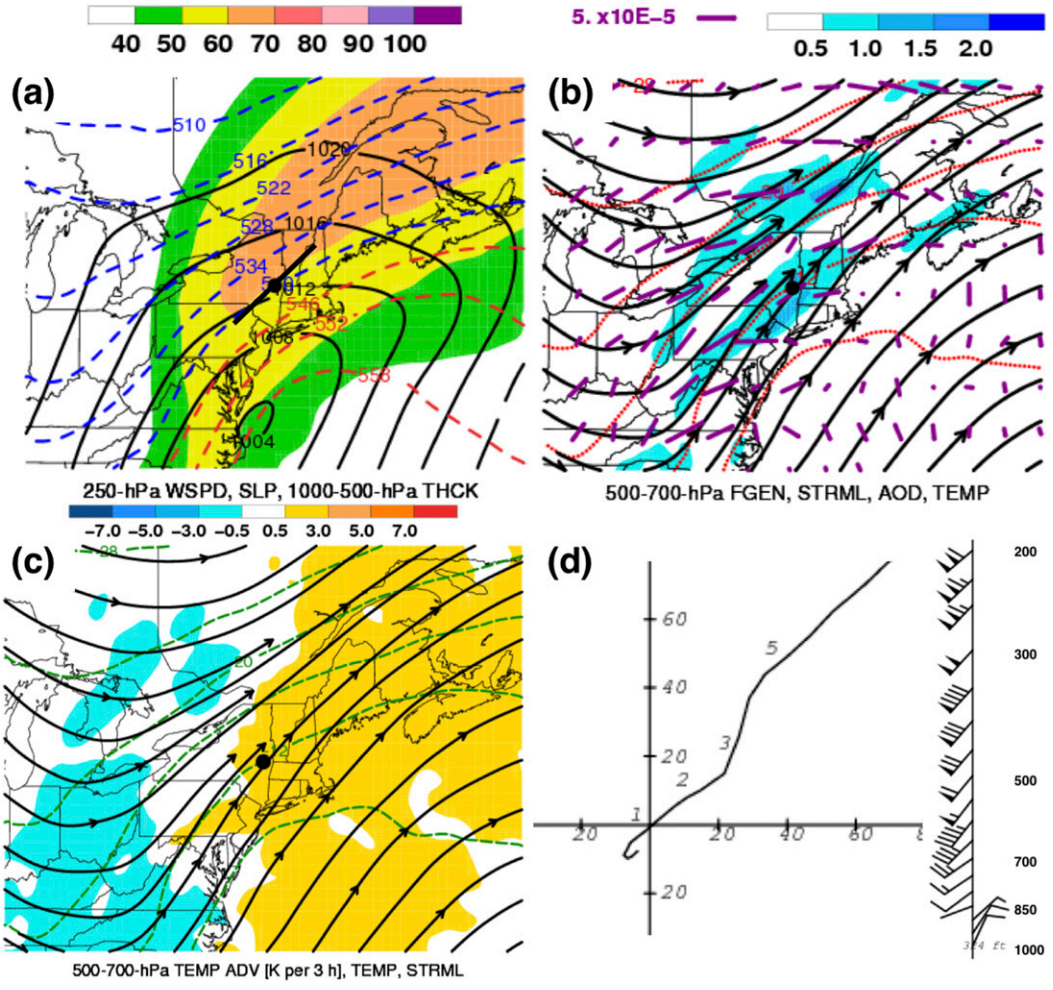

FIG. 7. As in Fig. 5, except for the laterally quasi-stationary category composite ($N = 8$).

entrance region of a southwest–northeast-oriented 250-hPa jet streak (Fig. 7a). The configuration of 1000–500-hPa thickness contours at the centroid implies an approximately southwest–northeast band orientation (Fig. 7a), which closely aligns with the composite-mean band orientation (i.e., 46° clockwise from the local meridian; Table 3). Frontogenesis in the 700–500-hPa layer is found near the centroid,

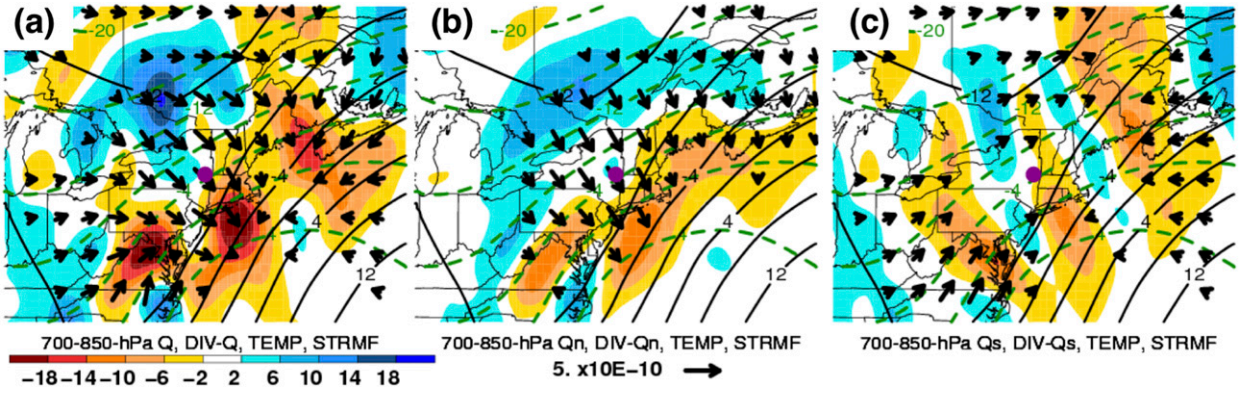

FIG. 8. As in Fig. 6, except for the laterally quasi-stationary category composite ($N = 8$). In all panels, the heavy purple dot marks the band centroid location.

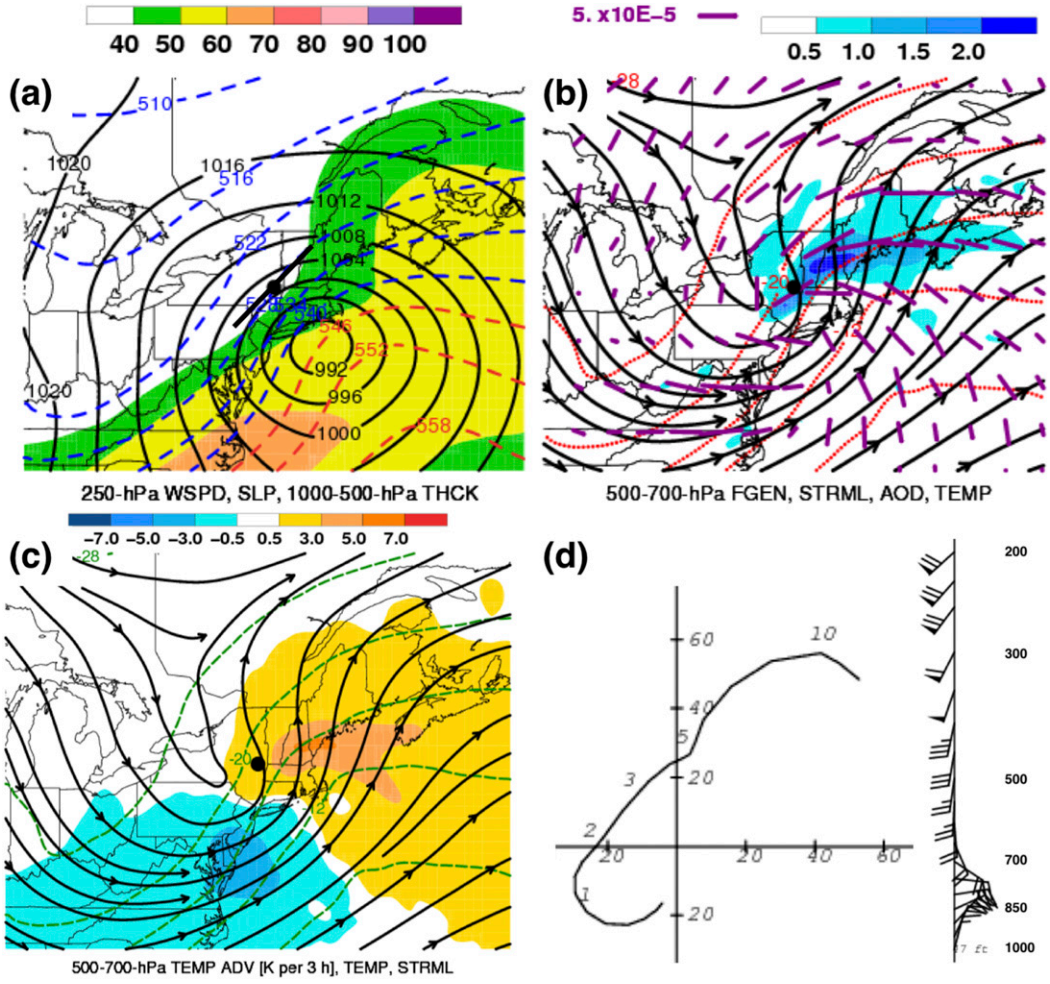

FIG. 9. As in Fig. 5, except for the pivoting category composite ($N = 18$). In (a)–(c), the heavy black dot marks the PZ location, which is the profile location for (d).

and a confluent asymptote is present along the cold side of the band axis (Fig. 7b). All bands in the composite are observed to move toward the northeast (i.e., in a largely along-axis direction), and this motion is associated with the small across-band component of the 700–500-hPa flow that may be inferred from Fig. 7b. Weak 700–500-hPa temperature advection is found at the centroid (Fig. 7c) and, as implied by the thermal wind, the vertical wind profile at the centroid yields an approximately straight and radially oriented hodograph (Fig. 7d).

In the vicinity of the centroid of the composite laterally quasi-stationary snowband, 850–700-hPa $\mathbf{Q}$ generally exhibits a more prominent across-isotherm contribution than along-isotherm contribution, and surrounding the centroid $\nabla_p \cdot \mathbf{Q}$ attains large magnitudes relative to background values (Fig. 8a). The orientation of $\mathbf{Q}_n$ toward warmer air is in the sense of an increase of $|\nabla_p \theta|$ by the nondivergent wind, and the elongated region of $\mathbf{Q}_n$ convergence provides QG forcing of ascent associated with a frontal circulation (Fig. 8b; compare the distribution of $\mathbf{Q}_n$ convergence with its counterpart in Fig. 2b, lower panel). Within a distance of ~300 km upshear and downshear of the centroid, $\mathbf{Q}_s$ exhibits small magnitudes relative to background values, indicative of a relatively weak rotation of $\nabla_p \theta$ by the nondivergent wind along much of the composite band, and the distribution of $\nabla_p \cdot \mathbf{Q}_s$ surrounding the centroid is diffuse and unorganized (Fig. 8c).

3) PIVOTING CATEGORY COMPOSITE

The PZ of the composite pivoting snowband is located ~350 km northwest of the center of a surface cyclone and within the poleward-exit region of a southwest–northeast-oriented 250-hPa jet streak (Fig. 9a). The configuration of 1000–500-hPa thickness contours at the PZ implies an approximately southwest–northeast band orientation (Fig. 9a), which aligns closely with the composite-mean band orientation (i.e., 44° clockwise

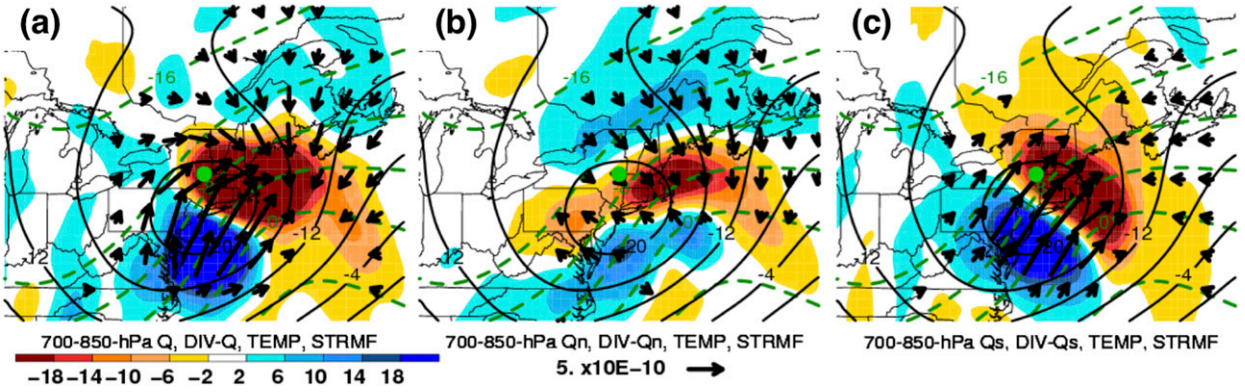

FIG. 10. As in Fig. 6, except for the pivoting category composite (N = 18). In all panels, the heavy green dot marks the PZ location.

from the local meridian; Table 3), and all bands in the composite are observed to rotate counterclockwise. Frontogenesis in the 700–500-hPa layer near the PZ is associated with deformation in diffluent flow located downstream of a negatively tilted trough axis (Fig. 9b). A dipole of 700–500-hPa temperature advection is oriented in the layer-mean along-isotherm direction, and warm advection is present at the PZ (Fig. 9c). As implied by the thermal wind, the vertical wind profile at the PZ exhibits veering with height (Fig. 9d).

In the vicinity of the PZ, 850–700-hPa $\mathbf{Q}$ exhibits both across- and along-isotherm contributions, and $\nabla_p \cdot \mathbf{Q}$ features a prominent dipole (Fig. 10a). The orientation of $\mathbf{Q}_n$ is primarily toward warmer (colder) air in the region downshear (upshear) of the PZ (Fig. 10b), indicating an increase (decrease) of $|\nabla_p\theta|$ by the nondivergent wind. This distribution of $\mathbf{Q}_n$ yields an elongated region of $\mathbf{Q}_n$ convergence, flanked by regions of $\mathbf{Q}_n$ divergence (Fig. 10b; compare the distribution of $\mathbf{Q}_n$ convergence with its counterpart in Fig. 2b, lower panel). In the vicinity of the PZ, $\mathbf{Q}_s$ attains large magnitudes relative to background values and $\mathbf{Q}_s$ is oriented downshear, implying a counterclockwise rotation of $\nabla_p\theta$ by the nondivergent wind (Fig. 10c). A prominent dipole of $\nabla_p \cdot \mathbf{Q}_s$ is located in the vicinity of the PZ (Fig. 10c; compare the dipole of $\nabla_p \cdot \mathbf{Q}_s$ with its counterpart in Fig. 2c, lower panel). Comparison of Fig. 10a with Fig. 10c shows that the aforementioned $\nabla_p \cdot \mathbf{Q}$ dipole may be attributed primarily to the $\nabla_p \cdot \mathbf{Q}_s$ dipole, which is augmented by the elongated region of $\mathbf{Q}_n$ convergence and the flanking region of $\mathbf{Q}_n$ divergence located in the southeastern quadrant of the 850–700-hPa cyclone (Fig. 10b).

b. Case studies

1) Laterally translating snowband

At 0600 UTC 9 December 2009, a laterally translating snowband extends from south-central New York to western Long Island and adjacent coastal waters, with the band centroid located over northern New Jersey (Fig. 11a). The band is progressing northeastward at ~15 m s^{-1} (refer to Fig. 3a and the animated radar mosaic provided in the online supplemental material), and numerous stations traversed by the band report moderate snow (not shown). In association with the largely across-axis motion of the band, 24-h snowfall accumulation ending at 1200 UTC 9 December 2009 is relatively uniform (i.e., generally ~10–15 cm) across much of the region traversed by the band, particularly from north-central Pennsylvania into southern New York (Fig. 4a). The abrupt tapering of snowfall toward the southeast in Fig. 4a is primarily attributable to a rain–snow line, as revealed by surface observations (not shown).

The band centroid at 0600 UTC 9 December 2009 is located east of the center of a surface cyclone and within the equatorward entrance region of a 250-hPa jet streak (Fig. 11a). The configuration of 1000–500-hPa thickness contours at the centroid aligns closely with the northwest–southeast band orientation (Fig. 11a). Frontogenesis in the 700–500-hPa layer near the centroid is associated with deformation in diffluent southwesterly flow (Fig. 11b), and the observed motion of the band toward the northeast is associated with the large across-band component of the 700–500-hPa flow that may be inferred from Fig. 11b. The centroid is located within a region of 700–500-hPa warm advection and immediately northeast of a warm-advection maximum (Fig. 11c). As implied by the thermal wind, the vertical wind profile at the centroid exhibits veering with height (Fig. 11d).

In the vicinity of the band centroid at 0600 UTC 9 December 2009, 850–700-hPa $\mathbf{Q}$ exhibits both across- and along-isotherm contributions, and $\nabla_p \cdot \mathbf{Q}$ attains large magnitudes relative to background values (Fig. 12a). The orientation of $\mathbf{Q}_n$ toward warmer air in the vicinity of the centroid indicates that the nondivergent wind contributes to an increase of $|\nabla_p\theta|$, and

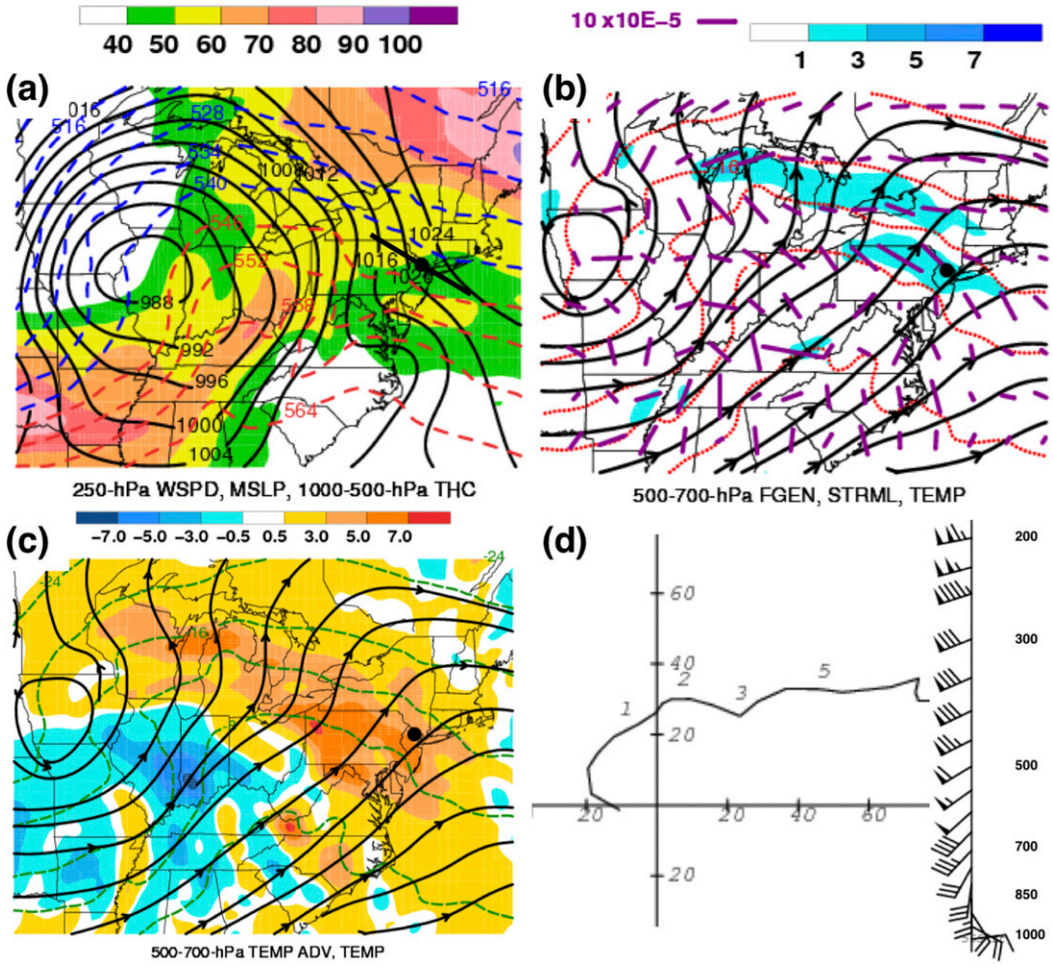

FIG. 11. As in Fig. 5, except for the laterally translating snowband at 0600 UTC 9 Dec 2009. In (a), the black line segment represents the position of the band axis and corresponds to the dash–dot pattern in Fig. 3a. In (b), the reference axis of dilatation (representing a resultant deformation of $10 \times 10^{-5}\,\mathrm{s}^{-1}$) and Miller 2D frontogenesis color bar have been rescaled from Fig. 5b.

the elongated region of $\mathbf{Q}_n$ convergence provides QG forcing of ascent associated with a frontal circulation (Fig. 12b). The orientation of $\mathbf{Q}_s$ in the region upshear (downshear) of the centroid indicates a counterclockwise (clockwise) rotation of $\nabla_p\theta$ by the nondivergent wind, yielding a region of $\mathbf{Q}_s$ convergence that is maximized upshear of the centroid (Fig. 12c). Within this region of $\mathbf{Q}_s$ convergence and upshear of the centroid, the magnitude of $\mathbf{Q}_s$ is small relative to where $\mathbf{Q}_s$ is oriented downshear and upshear surrounding the centroid (Fig. 12c), indicative of a relatively weak rotation of $\nabla_p\theta$ by the nondivergent wind.

2) LATERALLY QUASI-STATIONARY SNOWBAND

At 0600 UTC 2 March 2009, a laterally quasi-stationary snowband extends from northern New Jersey to far southwestern Maine, with the band centroid located over northwestern Connecticut (Fig. 13a). This band is progressing northeastward along its axis and impacting a narrow corridor (refer to Fig. 3c and the animated radar mosaic provided in the online supplemental materials), where numerous stations report moderate snow over a ~3-h period (not shown). In association with the largely along-axis motion of the band, 24-h snowfall accumulation ending at 1200 UTC 2 March 2009 reveals a southwest–northeast corridor of heavy accumulation (locally >20 cm) within the region traversed by the band (Fig. 4c). Accumulation southeast of this corridor is somewhat lighter (i.e., generally ~15–20 cm), while accumulation tapers markedly northwest of this corridor, where many locations within ~50 km of this corridor receive <4 cm of accumulation, resulting in a pronounced gradient of snowfall accumulation (Fig. 4c).

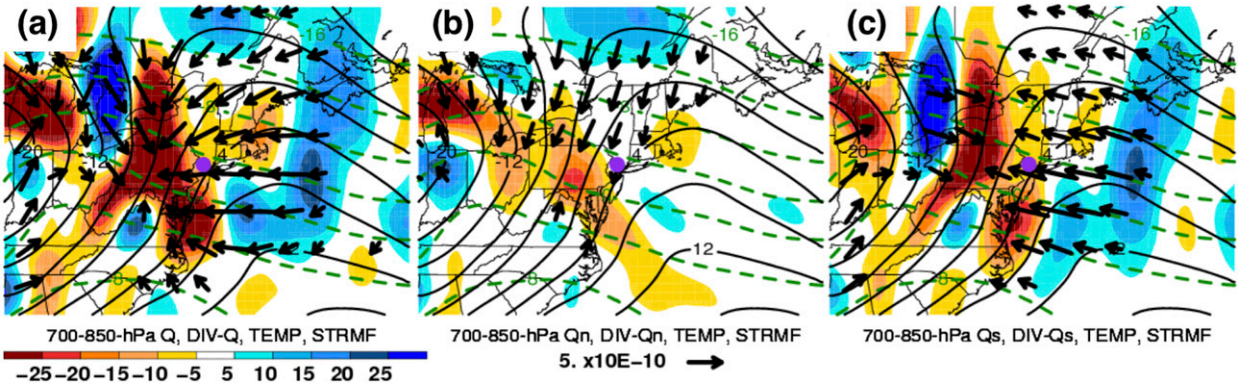

FIG. 12. As in Fig. 6, except for the laterally translating snowband at 0600 UTC 9 Dec 2009. The **Q** with magnitude $\geq 2 \times 10^{-10}$ K m^{-1} s^{-1} is plotted, and the **Q**-divergence color bar has been rescaled from Fig. 6. In all panels, the heavy purple dot marks the band centroid location.

The band centroid at 0600 UTC 2 March 2009 is located north of the center of a surface cyclone and within the equatorward entrance region of a southwest–northeast-oriented 250-hPa jet streak (Fig. 13a). The configuration of 1000–500-hPa thickness contours at the centroid aligns closely with the southwest–northeast band orientation (Fig. 13a). Frontogenesis in the 700–500-hPa layer is found near the centroid, and a confluent asymptote, extending from western New York to southeastern Quebec, is present along the cold side of the band axis (Fig. 13b). The observed motion of the band toward the northeast is associated with the small across-band component of the 700–500-hPa flow that may be inferred from Fig. 13b. Weak 700–500-hPa temperature advection is found at the centroid (Fig. 13c) and, as implied by the thermal wind, the vertical wind profile at the centroid yields an approximately straight and radially oriented hodograph (Fig. 13d).

In the vicinity of the centroid at 0600 UTC 2 March 2009, 850–700-hPa **Q** exhibits a more prominent across-isotherm contribution than along-isotherm contribution, and surrounding the centroid $\nabla_p \cdot \mathbf{Q}$ attains large magnitudes relative to background values (Fig. 14a). The orientation of $\mathbf{Q}_n$ toward warmer air in the vicinity of the centroid indicates an increase of $|\nabla_p \theta|$ by the nondivergent wind, and the elongated region of $\mathbf{Q}_n$ convergence provides QG forcing of ascent associated with a frontal circulation (Fig. 14b). Within a distance of ~300 km upshear and ~100 km downshear of the centroid, $\mathbf{Q}_s$ exhibits small magnitudes relative to background values, indicative of a relatively weak rotation of $\nabla_p \theta$ by the nondivergent wind, and $\nabla_p \cdot \mathbf{Q}_s$ surrounding the centroid is unorganized and lacking coherence (Fig. 14c).

3) PIVOTING SNOWBAND

At 1200 UTC 12 February 2006, a pivoting snowband extends from Chesapeake Bay to far southeastern New Hampshire, with the PZ located over northern Connecticut (Figs. 3d and 15a). The band axis is rotating counterclockwise (refer to Fig. 3d and the animated radar mosaic provided in the online supplemental material), and several stations traversed by the band report heavy snow over a ~5-h period (not shown). The 24-h snowfall-accumulation pattern ending at 1800 UTC 12 February 2006 reveals a southwest–northeast corridor of heavy accumulation (locally >50 cm; Fig. 4d). Accumulation tapers markedly toward the northwest of this corridor, generally to amounts < 10 cm within a distance of ~40 km from this corridor, resulting in a pronounced gradient of snowfall accumulation (Fig. 4d). Additional analysis of the 12 February 2006 snowband and the evolution of the band environment is provided by Novak et al. (2009, section 5).

At 1200 UTC 12 February 2006, the PZ is located north-northwest of the center of a surface cyclone and within the poleward-exit region of a southwest–northeast-oriented 250-hPa jet streak (Fig. 15a). The configuration of 1000–500-hPa thickness contours at the PZ aligns closely with the southwest–northeast band orientation (Fig. 15a). Frontogenesis in the 700–500-hPa layer near the PZ is associated with deformation in diffluent flow located downstream of a negatively tilted trough axis (Fig. 15b). An asymmetric dipole of 700–500-hPa temperature advection is oriented in the layer-mean along-isotherm direction, and warm advection is present at the PZ (Fig. 15c). As implied by the thermal wind, the vertical wind profile at the PZ exhibits veering with height below ~5 km AGL (Fig. 15d; note that a low-level speed maximum extends a portion of the hodograph beyond the range of the plot).

In the vicinity of the PZ at 1200 UTC 12 February 2006, 850–700-hPa **Q** exhibits both across- and along-isotherm contributions, and $\nabla_p \cdot \mathbf{Q}$ features a prominent dipole (Fig. 16a). The orientation of $\mathbf{Q}_n$ is primarily

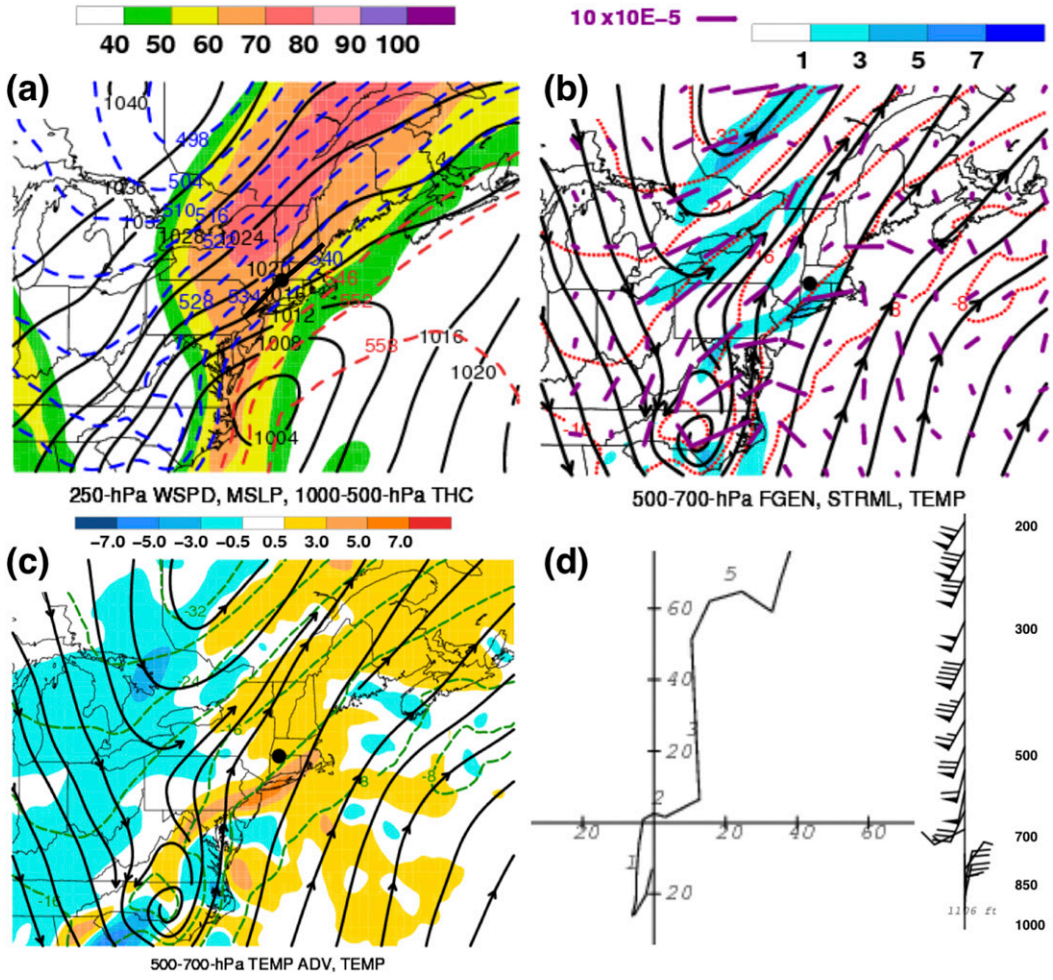

FIG. 13. As in Fig. 11, except for the laterally quasi-stationary snowband at 0600 UTC 2 Mar 2009. In (a), the black line segment represents the position of the band axis and corresponds to the dash–dot pattern in Fig. 3c.

toward warmer (colder) air in the region downshear (upshear) of the PZ, indicating an increase (decrease) of $|\nabla_p\theta|$ by the nondivergent wind, and a region of $\mathbf{Q}_n$ convergence is flanked by regions of $\mathbf{Q}_n$ divergence (Fig. 16b). In the vicinity of the PZ, $\mathbf{Q}_s$ attains large magnitudes relative to background values and $\mathbf{Q}_s$ is oriented downshear, implying a counterclockwise rotation of $\nabla_p\theta$ by the nondivergent wind (Fig. 16c). A dipole of $\nabla_p \cdot \mathbf{Q}_s$ is located in the vicinity of the PZ (Fig. 16c), and this $\nabla_p \cdot \mathbf{Q}_s$ dipole comprises the dominant contribution to the aforementioned $\nabla_p \cdot \mathbf{Q}$ dipole in Fig. 16a.

4. Discussion

a. Conceptual models

The foregoing composites and case studies indicate that the motion of mesoscale snowbands that are forced by frontogenesis is related to features of the band environment, such as band position relative to surface cyclones and upper-level jet streaks, the confluence/diffluence and curvature of midlevel streamlines, and the distribution of horizontal temperature advection. Band motion is also related to hodograph shape, as well as to the across- and along-isotherm components of $\mathbf{Q}$. The snowband-motion category composites are distinct from each other, suggesting that the classification scheme employed in the present study has utility not only as a means for describing band motion, but also as a framework for relating band motion to the band environment. The composites and their associated case studies are the basis for the conceptual models in Figs. 17a–c, which synthesize the features of the band environment commonly associated with laterally translating, laterally quasi-stationary, and pivoting snowbands, respectively.

In the laterally translating snowband conceptual model (Fig. 17a), a band oriented approximately west-northwest–east-southeast exhibits largely across-axis

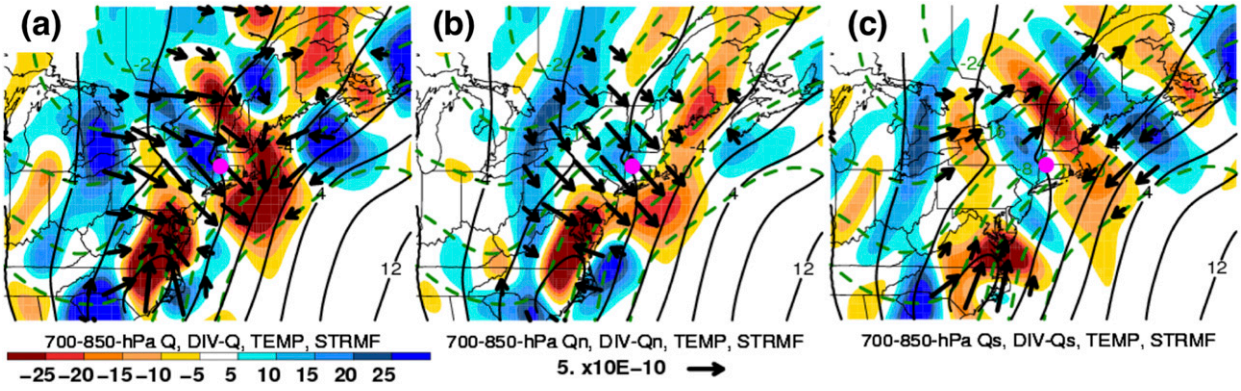

FIG. 14. As in Fig. 12, except for the laterally quasi-stationary snowband at 0600 UTC 2 Mar 2009. In all panels, the heavy magenta dot marks the band centroid location.

motion toward the north-northeast, with the centroid located east-northeast of the center of a surface cyclone and within the equatorward-entrance region of an upper-level jet streak. Near the centroid, midlevel frontogenesis is associated with diffluent southwesterly flow, a large across-band component of the midlevel flow, and warm advection, yielding a veering wind profile with height at the centroid. The association of laterally translating snowbands with a large across-band component of the midlevel flow is consistent with the findings of Harper and Beimers (1958) and Seltzer et al. (1985). In the vicinity of the centroid, low-level $\mathbf{Q}_n$ is oriented toward warmer air, and an elongated region of $\mathbf{Q}_n$ convergence provides QG forcing of ascent associated with a frontal circulation. Additional forcing of ascent and differential rotation of $\nabla_p\theta$ are indicated by a region of $\mathbf{Q}_s$ convergence that encompasses the centroid. This region of $\mathbf{Q}_s$ convergence is approximately centered between $\mathbf{Q}_s$ of opposing direction (i.e., where $\mathbf{Q}_s$ vanishes), such that the magnitude of $\mathbf{Q}_s$ at the centroid is small relative to where $\mathbf{Q}_s$ is oriented downshear and upshear surrounding the centroid. Accordingly, rotation of $\nabla_p\theta$ by the nondivergent wind is relatively weak at the centroid.

Similar to the laterally translating category composite, the ''east'' class composite of Novak (2002), consisting of snowband events in the eastern semicircle of surface cyclones, depicts midlevel frontogenesis associated with diffluent southwesterly flow and warm advection, with band motion commonly toward the northeast (i.e., in a largely across-axis direction). These similarities between the laterally translating category composite and the east class composite of Novak (2002) suggest that the two composites are consistent descriptions of snowbands in the eastern semicircle of surface cyclones, but which derive from complementary methods: Novak (2002) composites bands on the basis of cyclone-relative position and finds common band-motion characteristics, whereas the present study composites bands on the basis of band motion and finds a common cyclone-relative position.

In the laterally quasi-stationary snowband conceptual model (Fig. 17b), a band oriented approximately southwest–northeast exhibits largely along-axis motion toward the northeast, with the centroid located north-northeast of the center of a surface cyclone and within the equatorward-entrance region of an upper-level jet streak. A midlevel confluent asymptote is present along the cold side of the band axis and, near the centroid, midlevel frontogenesis is associated with a small across-band component of the midlevel flow and weak temperature advection, yielding an approximately straight, radially oriented hodograph at the centroid. In the vicinity of the centroid, low-level $\mathbf{Q}_n$ is oriented toward warmer air, and an elongated region of $\mathbf{Q}_n$ convergence provides QG forcing of ascent associated with a frontal circulation. The magnitude of $\mathbf{Q}_s$ along a substantial portion of the snowband (i.e., within ~100–300 km upshear and downshear of the centroid) is small relative to background values, and $\mathbf{Q}_s$ convergence surrounding the centroid is unorganized.

An environment characterized by relatively small-magnitude $\mathbf{Q}_s$ appears to be favorable for the occurrence of laterally quasi-stationary snowbands, since rotation of $\nabla_p\theta$ would contribute to rotation of the band itself, thereby precluding laterally quasi-stationary band motion. The association of laterally quasi-stationary snowbands with relatively small-magnitude $\mathbf{Q}_s$ corroborates the hypothesis of Banacos (2003), who postulates, but does not demonstrate, that stationary mesoscale bands (i.e., bands that would be termed laterally quasi-stationary in the present study) are associated with small-magnitude $\mathbf{F}_s$ (i.e., the $\mathbf{Q}_s$ analog employing the

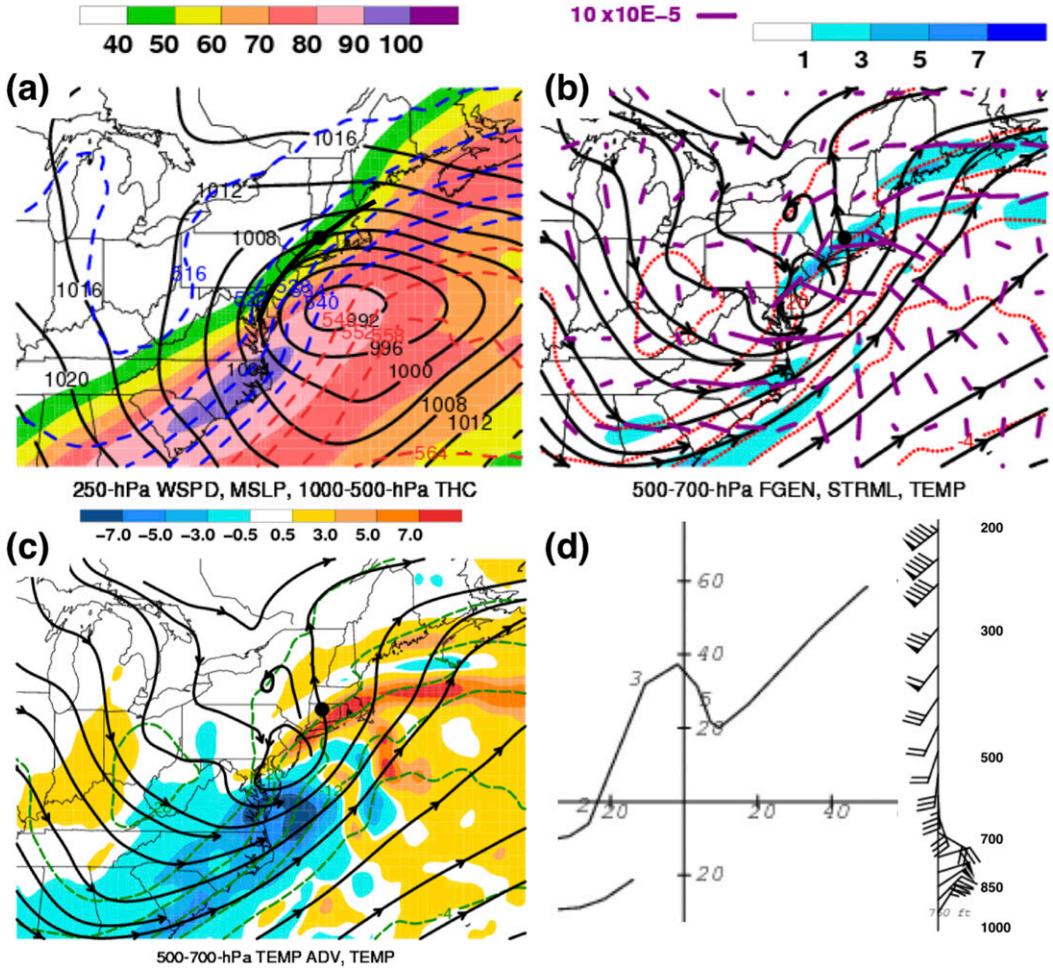

FIG. 15. As in Fig. 11, except for the pivoting snowband at 1200 UTC 12 Feb 2006. In (a), the black line segment represents the position of the band axis and corresponds to the dash–dot pattern in Fig. 3d. In (a)–(c), the heavy black dot marks the PZ location.

total horizontal wind). Moreover, Banacos (2003) observes that environments of stationary mesoscale bands often exhibit straight, radially oriented hodographs that approximately intersect the coordinate origin. The origin intersection, manifesting stagnation at a level above the surface, is associated with a horizontal col (Banacos 2003). Although the hodographs in the laterally quasi-stationary category composite and case study intersect the origin (see Figs. 7d and 13d, respectively), only three of the eight member events in the composite are associated with an 850–700-hPa layer-mean col within 100 km of the centroid (not shown). Therefore, the hodograph at the centroid in the laterally quasi-stationary snowband conceptual model is approximately straight and radially oriented, with or without intersecting the origin (refer to Fig. 17b, left-hand panel). Ganetis et al. (2018, p. 3680) note that their "parallel" band subcategory, characterized by along-axis band motion, is analogous to the laterally quasi-stationary category, and find that parallel bands are often observed in the northeast quadrant of developing surface cyclones.

In the pivoting snowband conceptual model (Fig. 17c), a band oriented approximately southwest–northeast exhibits pronounced counterclockwise rotation about the PZ, with the PZ located northwest of the center of a surface cyclone and within the poleward-exit region of an upper-level jet streak. Near the PZ, midlevel frontogenesis is associated with diffluent flow located downstream of a negatively tilted trough axis. A dipole of midlevel temperature advection is oriented in the along-isotherm direction, and warm advection is present at the PZ, yielding a veering wind profile with height at the PZ. Low-level $\mathbf{Q}_n$ is oriented primarily toward warmer (colder) air in the region downshear (upshear) of the PZ, yielding an elongated region of $\mathbf{Q}_n$ convergence and associated forcing of ascent. In the vicinity

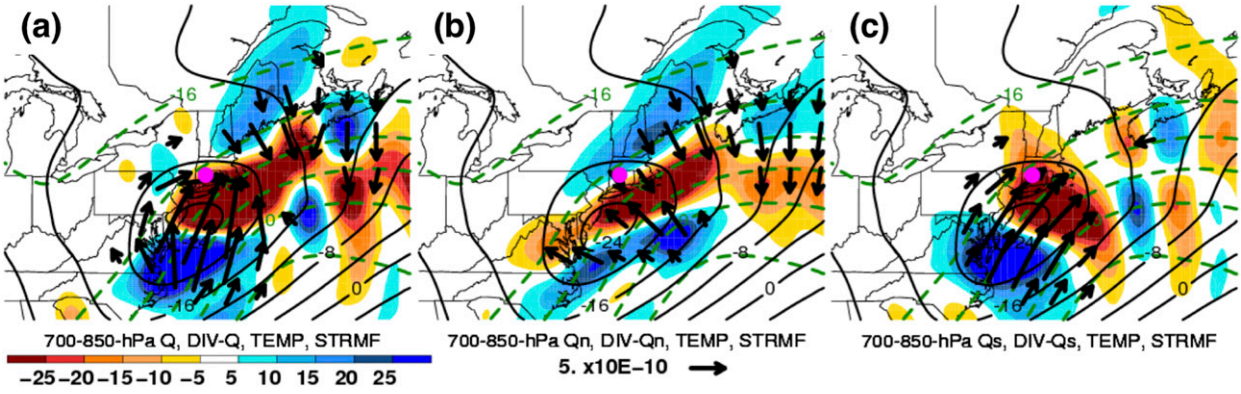

FIG. 16. As in Fig. 12, except for the pivoting snowband at 1200 UTC 12 Feb 2006. In all panels, the heavy magenta dot marks the PZ location.

of the PZ, $\mathbf{Q}_s$ exhibits large magnitudes relative to background values and is oriented downshear, and a dipole of $\nabla_p \cdot \mathbf{Q}_s$ is present in this region.

An environment characterized by relatively large-magnitude, downshear-oriented $\mathbf{Q}_s$ appears to be favorable for the occurrence of counterclockwise-pivoting snowbands, since this sense of band rotation would arise from a counterclockwise rotation of $\nabla_p\theta$ at the PZ. Moreover, $\mathbf{Q}_s$ convergence in the vicinity of the PZ, associated with the aforementioned dipole of $\nabla_p \cdot \mathbf{Q}_s$ (refer to Fig. 17c, right-hand panel), indicates differential rotation of $\nabla_p\theta$ by the nondivergent wind and QG forcing of ascent, and this forcing is present in addition to that provided by $\mathbf{Q}_n$ convergence in the vicinity of the PZ. Martin (1999) demonstrates that differential rotation of $\nabla_p\theta$ by $\mathbf{Q}_s$ is present in the northwest quadrant of cyclones during occlusion, and the present study suggests that the same mechanism is associated with pivoting snowband motion. Similar to the pivoting category composite, the ''northwest'' class composite of Novak (2002) and Novak et al. (2004), consisting of snowband events in the northwestern quadrant of surface cyclones, depicts midlevel frontogenesis associated with diffluent flow downstream of a negatively tilted trough axis and on the periphery of a warm-advection region, with bands often exhibiting ''an identifiable pivot point'' (Novak et al. 2004, p. 999). These similarities between the pivoting category composite and the northwest class composite of Novak (2002) and Novak et al. (2004) suggest that the two composites are consistent descriptions of snowbands in the northwestern quadrant of surface cyclones.

Because hybrid snowbands were found in various synoptic environments, a hybrid category composite and an associated conceptual model were not constructed. While lacking an associated conceptual model, the hybrid category is an explicitly defined category of band motion, characterized by an intermediate range of the angle β, which provides a metric of lateral motion, between that of the laterally quasi-stationary and laterally translating categories (refer to Fig. 1b). We hypothesize that a much larger sample of hybrid snowband events than the sample of seven events considered in this study might facilitate the identification of coherent subcategories of hybrid snowbands, from which composites could be constructed. Investigation of this hypothesis is suggested for future work.

b. *Applications to operational forecasting*

The conceptual models in Fig. 17 are intended to facilitate the forecasting process when mesoscale snowband formation is anticipated. Although the conceptual models depict spatial relationships between features of the band environment, it is worth emphasizing that these snowband-motion conceptual models are not predictions of band dimensions or of exact band position, since relating band position to a frontogenesis region is often not straightforward. This difficulty arises because frontogenesis is often vertically tilted, and the horizontal scale of the associated frontal circulation is modulated by the moist symmetric stability (e.g., Sawyer 1956; Sanders and Bosart 1985; Novak et al. 2006). Moreover, the lofting and horizontal advection of hydrometeors may displace a snowband from a region of ascent (Novak et al. 2008). Nevertheless, the identification of low- to midlevel frontogenesis collocated with moisture and weak moist symmetric stability will often aid in determining a region and timeframe in which mesoscale snowbands are most likely to develop (Novak et al. 2006). Band motion can then be anticipated by considering the features of the environment near a frontogenesis region, using Fig. 17 as an aid, even if the exact band position is uncertain.

Laterally quasi-stationary and pivoting snowbands may favor sharp snowfall-accumulation gradients,

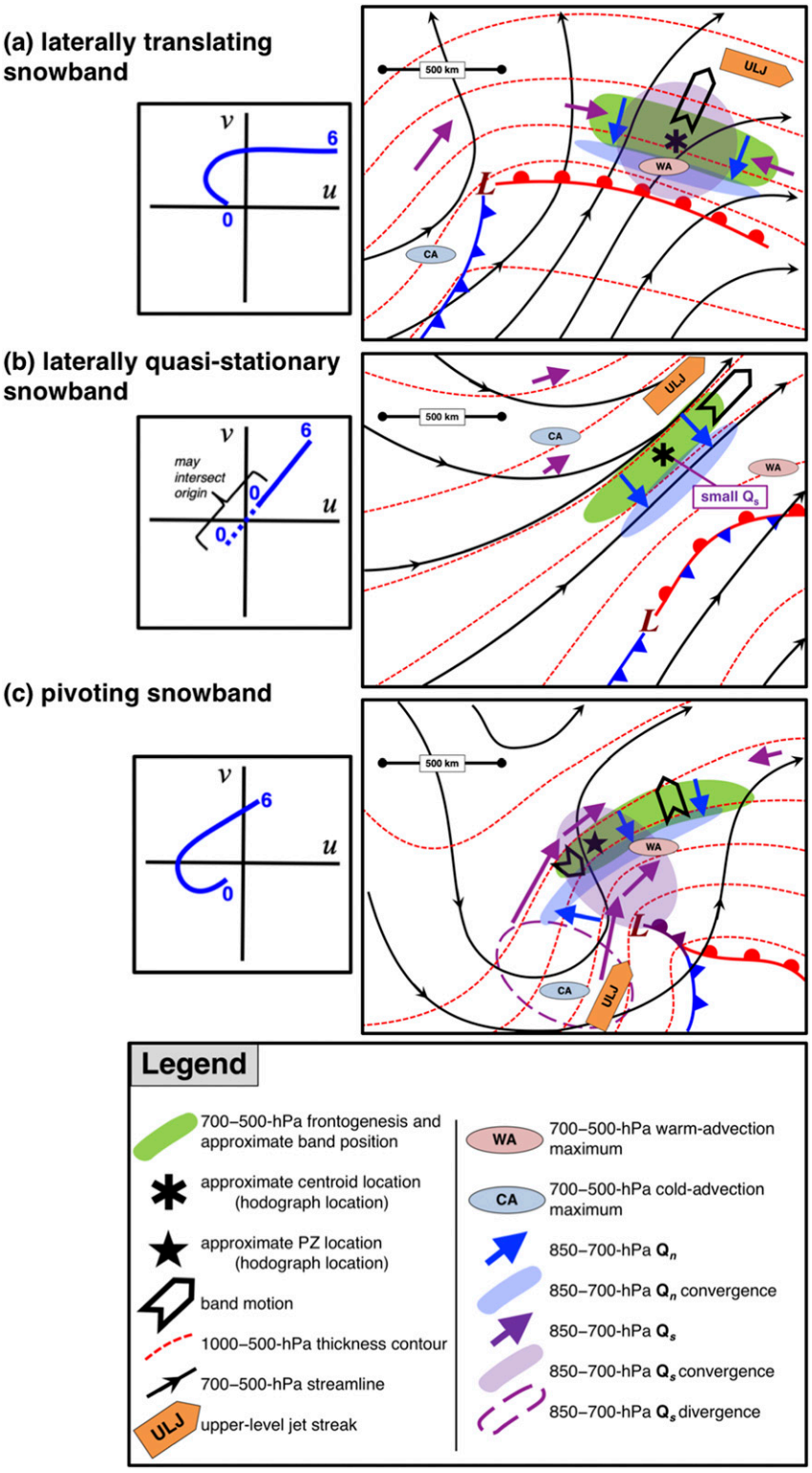

FIG. 17. Conceptual models for the (a) laterally translating snowband, (b) laterally quasi-stationary snowband, and (c) pivoting snowband. Features are shown according to legend at bottom; other symbols are conventional. For each right-hand panel, the hodograph at the centroid or PZ location (whichever is applicable) is shown in the corresponding left-hand panel, where "0" and "6" correspond to 0 and 6 km AGL, respectively.

since band residence time and associated heavy snow will be prolonged either 1) along the band axis in cases of laterally quasi-stationary bands, or 2) along a region traversed by the PZ in cases of pivoting bands. Immediately adjacent to these regions of heavy snow, snowfall accumulation may be considerably lighter. Thus, when laterally quasi-stationary or pivoting snowbands are anticipated, errors in snowfall-accumulation forecasts will be sensitive to displacement errors in snowband-position forecasts. In these situations, certain aspects of the forecast may be qualified with statements of uncertainty (e.g., ''there is high confidence that total accumulations will taper sharply from southeast to northwest, but low confidence on where the maximum accumulations will occur''). On the other hand, laterally translating snowbands may also be associated with heavy snowfall rates, but forecasts of snowfall accumulation will be less sensitive to displacement errors in snowband-position forecasts, owing to the across-axis motion of these bands and the transient nature of heavy snow associated with them.

We hypothesize that snowband motion is accurately represented in deterministic convection-allowing models (CAMs), given that the snowband environments depicted in Fig. 17 are distinct from each other on horizontal scales that are well resolved by CAMs, and given that high-resolution models can produce realistic representations of snowband evolution (Novak et al. 2008). In a model-ensemble framework, we hypothesize that snowband-position uncertainty in the across-axis direction more strongly influences the snowfall-accumulation uncertainty in conjunction with laterally quasi-stationary and pivoting snowbands than with laterally translating snowbands. Investigation of these hypotheses is suggested for future work.

5. Summary

This study investigates environmental features associated with particular categories of snowband motion that are observed in northeast U.S. winter storms. Using radar reflectivity data, snowbands during a 6-yr period are subjectively identified and categorized according to a band motion classification scheme, wherein bands are classified as *laterally translating, hybrid, laterally quasi-stationary,* or *pivoting*. Composite analysis and case studies are utilized to ascertain the environmental features associated with laterally translating, laterally quasi-stationary, and pivoting bands. From this analysis, all snowbands are found to be associated with frontogenesis and QG forcing of ascent arising from the convergence of $\mathbf{Q}_n$, the across-isotherm contribution to the $\mathbf{Q}$ vector. Differences in snowband motion are found to be related to features of the band environment, including band position relative to surface cyclones and upper-level jet streaks, the confluence/diffluence and curvature of midlevel streamlines, the distribution of horizontal temperature advection, and hodograph shape. Differences in snowband motion are also found to be related to the magnitude of $\mathbf{Q}_s$, the along-isotherm contribution to the $\mathbf{Q}$ vector, and to the distribution of $\nabla_p \cdot \mathbf{Q}_s$.

Operational forecasting procedures applicable to mesoscale snowbands typically emphasize the accurate anticipation of band position and snowfall rate in the preparation of snowfall-accumulation forecasts. While this emphasis is warranted, the authors posit that band motion should also be considered during the forecasting process, since band-motion characteristics may serve to either mitigate or augment the snowfall-accumulation errors that stem from errors in band position and/or snowfall rate. The present study builds upon the existing literature on mesoscale snowbands by describing band motion more comprehensively, and by relating band motion to features of the band environment and the resulting distribution of snowfall accumulation.

Acknowledgments. The authors are grateful to the Northeast Regional Climate Center and Southeast Regional Climate Center for assistance in gathering PLCD site records, and to Dr. John M. Brown (NOAA/ESRL) and three anonymous reviewers for providing constructive comments that improved this manuscript. This research was supported by NOAA Grants NA01NWS4680002 and NA16NWS4680005, awarded to the University at Albany, SUNY, as part of the Collaborative Science, Technology, and Applied Research program.

REFERENCES

Banacos, P. C., 2003: Short range prediction of banded precipitation associated with deformation and frontogenetical forcing. Preprints, *10th Conf. on Mesoscale Processes*, Portland, OR, Amer. Meteor. Soc., P1.7.

Baxter, M. A., and P. N. Schumacher, 2017: Distribution of single-banded snowfall in central U.S. cyclones. *Wea. Forecasting*, **32**, 533–554, https://doi.org/10.1175/WAF-D-16-0154.1.

desJardins, M. L., K. F. Brill, and S. S. Schotz, 1991: Use of GEMPAK on UNIX workstations. *Proc. Seventh Int. Conf. on Interactive Information and Processing Systems for Meteorology, Oceanography, and Hydrology,* New Orleans, LA, Amer. Meteor. Soc., 449–453.

Doswell, C. A., III, H. E. Brooks, and R. A. Maddox, 1996: Flash flood forecasting: An ingredients-based methodology. *Wea. Forecasting*, **11**, 560–581, https://doi.org/10.1175/1520-0434(1996)011<0560:FFFAIB>2.0.CO;2.

Eliassen, A., 1962: On the vertical circulation in frontal zones. *Geofys. Publ.*, **24**, 147–160.

Evans, M., and M. L. Jurewicz Sr., 2009: Correlations between analyses and forecasts of banded heavy snow ingredients and observed snowfall. *Wea. Forecasting*, **24**, 337–350, https://doi.org/10.1175/2008WAF2007105.1.

Ganetis, S. A., B. A. Colle, S. E. Yuter, and N. P. Hoban, 2018: Environmental conditions associated with observed snowband structures within northeast U.S. winter storms. *Mon. Wea. Rev.*, **146**, 3675–3690, https://doi.org/10.1175/MWR-D-18-0054.1.

Harper, W. G., and J. G. D. Beimers, 1958: The movement of precipitation belts as observed by radar. *Quart. J. Roy. Meteor. Soc.*, **84**, 242–249, https://doi.org/10.1002/qj.49708436105.

Hoskins, B. J., and M. A. Pedder, 1980: The diagnosis of middle latitude synoptic development. *Quart. J. Roy. Meteor. Soc.*, **106**, 707–719, https://doi.org/10.1002/qj.49710645004.

——, I. Draghici, and H. C. Davies, 1978: A new look at the ω-equation. *Quart. J. Roy. Meteor. Soc.*, **104**, 31–38, https://doi.org/10.1002/qj.49710443903.

Kenyon, J. S., 2013: The motion of mesoscale snowbands in northeast U.S. winter storms. M.S. thesis, Dept. of Atmospheric and Environmental Sciences, University at Albany, State University of New York, 108 pp., http://www.atmos.albany.edu/student/jkenyon/Kenyon_thesis.pdf.

Keyser, D., M. J. Reeder, and R. J. Reed, 1988: A generalization of Petterssen's frontogenesis function and its relation to the forcing of vertical motion. *Mon. Wea. Rev.*, **116**, 762–781, https://doi.org/10.1175/1520-0493(1988)116<0762:AGOPFF>2.0.CO;2.

——, B. D. Schmidt, and D. G. Duffy, 1992: Quasigeostrophic vertical motions diagnosed from along- and cross-isentrope components of the Q vector. *Mon. Wea. Rev.*, **120**, 731–741, https://doi.org/10.1175/1520-0493(1992)120<0731:QVMDFA>2.0.CO;2.

Martin, J. E., 1999: Quasigeostrophic forcing of ascent in the occluded sector of cyclones and the trowal airstream. *Mon. Wea. Rev.*, **127**, 70–88, https://doi.org/10.1175/1520-0493(1999)127<0070:QFOAIT>2.0.CO;2.

Miller, J. E., 1948: On the concept of frontogenesis. *J. Meteor.*, **5**, 169–171, https://doi.org/10.1175/1520-0469(1948)005<0169:OTCOF>2.0.CO;2.

Nielsen-Gammon, J. W., and D. A. Gold, 2008: Dynamical diagnosis: A comparison of quasigeostrophy and Ertel potential vorticity. *Synoptic–Dynamic Meteorology and Weather Analysis and Forecasting: A Tribute to Fred Sanders, Meteor. Monogr.,* No. 55, Amer. Meteor. Soc., 183–202, https://doi.org/10.1175/0065-9401-33.55.183.

Novak, D. R., 2002: A climatological and composite study of cold season banded precipitation in the northeast United States. M.S. thesis, University at Albany, State University of New York, 182 pp. [Available from Dept. of Atmospheric and Environmental Sciences, University at Albany, State University of New York, Albany, NY 12222.]

——, L. F. Bosart, D. Keyser, and J. S. Waldstreicher, 2004: An observational study of cold season–banded precipitation in northeast U.S. cyclones. *Wea. Forecasting*, **19**, 993–1010, https://doi.org/10.1175/815.1.

——, J. S. Waldstreicher, D. Keyser, and L. F. Bosart, 2006: A forecast strategy for anticipating cold season mesoscale band formation within eastern U.S. cyclones. *Wea. Forecasting*, **21**, 3–23, https://doi.org/10.1175/WAF907.1.

——, B. A. Colle, and S. E. Yuter, 2008: High-resolution observations and model simulations of the life cycle of an intense mesoscale snowband over the northeastern United States. *Mon. Wea. Rev.*, **136**, 1433–1456, https://doi.org/10.1175/2007MWR2233.1.

——, ——, and R. McTaggart-Cowan, 2009: The role of moist processes in the formation and evolution of mesoscale snowbands within the comma head of northeast U.S. cyclones. *Mon. Wea. Rev.*, **137**, 2662–2686, https://doi.org/10.1175/2009MWR2874.1.

NWS, 2018: Climate records. National Weather Service Instruction 10-1004, 28 pp. [Available online at http://www.nws.noaa.gov/directives/sym/pd01010004curr.pdf.]

Saha, S., and Coauthors, 2010: The NCEP Climate Forecast System Reanalysis. *Bull. Amer. Meteor. Soc.*, **91**, 1015–1058, https://doi.org/10.1175/2010BAMS3001.1.

Sanders, F., and L. F. Bosart, 1985: Mesoscale structure in the Megalopolitan snowstorm of 11–12 February 1983. Part I: Frontogenetical forcing and symmetric Instability. *J. Atmos. Sci.*, **42**, 1050–1061, https://doi.org/10.1175/1520-0469(1985)042<1050:MSITMS>2.0.CO;2.

Sawyer, J. S., 1956: The vertical circulation at meteorological fronts and its relation to frontogenesis. *Proc. Roy. Soc. London*, **234A**, 346–362, https://doi.org/10.1098/rspa.1956.0039.

Seltzer, M. A., R. E. Passarelli, and K. A. Emanuel, 1985: The possible role of symmetric instability in the formation of precipitation bands. *J. Atmos. Sci.*, **42**, 2207–2219, https://doi.org/10.1175/1520-0469(1985)042<2207:TPROSI>2.0.CO;2.